Date 13th May 2011

UNIVERSITY OF CANTERBURY
Te Whare Wānanga o Waitaha
CHRISTCHURCH NEW ZEALAND

Modelling of shear sensitive cells in stirred tank reactor using computational fluid dynamics

A thesis submitted in partial fulfilment of the requirements for the Degree of

(Masters by Thesis in Chemical and Process Engineering)

in the University of Canterbury, Christchurch, New Zealand

by

(Harminder Singh)

Dedicated to the Almighty, One True Lord

Table of Contents

Table of Figures

Table of Tables

Acknowledgements

I would like to sincerely thank the Almighty, the One True Lord, for blessing the knowledge, will power, and skills required to become a researcher. During this process of becoming a researcher many obstacles have come, but the able guidance and critique that came through supervisor, Justin J. Nijdam and co-supervisor, Gabriel Visnovsky really helped in overcoming those obstacles and in the process of becoming not only a better researcher but a better human being as well.

I would also like to thank the technicians, namely, Tony Allen, Frank Weerts, Leigh Richardson, Glenn Wilson, David Brown, Bob Gordon and Peter Jones for the ideas and help throughout the course of the study. I am also grateful to all of the technicians, post-grads, and staff of the Chemical and Process Engineering department in making this an enjoyable place to work. Moreover, I would like to express gratitude for the staff of Learning Skills Centre, especially Darina Norwood, for helping in the improvement of written English skills. Finally, I would like to thank the family and friends for their support from the beginning to the end of this project.

Abstract

Animal cells are often cultured in stirred tank reactors. Having no cell wall, these animal cells are very sensitive to the fluid mechanical stresses that result from agitation by the impeller and from the rising and bursting of bubbles, which are generated within the culture medium in the stirred tank to supply oxygen by mass transfer to the cells. If excessive, these fluid mechanical stresses can result in damage/death of animal cells. Stress due to the rising and bursting of bubbles can be avoided by using a gas-permeable membrane, in the form of a long coiled tube (with air passing through it) within the stirred tank, instead of air-bubbles to oxygenate the culture medium. Fluid mechanical stress due to impeller agitation can be controlled using appropriate impeller rotational speeds. The aim of this study was to lay the foundations for future work in which a correlation would be developed between cell damage/death and the fluid mechanical stresses that result from impeller agitation and bubbling. Such a correlation could be used to design stirred-tank reactors at any scale and to determine appropriate operating conditions that minimise cell damage/death due to fluid mechanical stresses.

Firstly, a validated CFD model of a baffled tank stirred with a Rushton turbine was developed to allow fluid mechanical stresses due to impeller agitation to be estimated. In these simulations, special attention was paid to the turbulence energy dissipation rate, which has been closely linked to cell damage/death in the literature. Different turbulence models, including the k-ε, SST, SSG-RSM and the SAS-SST models, were investigated.

All the turbulence models tested predicted the mean axial and tangential velocities reasonably well, but under-predicted the decay of mean radial velocity away from the impeller. The k-ε model predicted poorly the generation and dissipation of turbulence in the vicinity of the impeller. This contrasts with the SST model, which properly predicted the appearance of maxima in the turbulence kinetic energy and turbulence energy dissipation rate just off the impeller blades. Curvature correction improved the SST model by allowing a more accurate prediction of the magnitude and location of these maxima. However, neither the k-ε nor the SST models were able to properly capture the chaotic and three-dimensional nature of the trailing vortices that form downstream of the blades of the impeller. In this sense, the SAS-SST model produced more physical predictions. However,

this model has some drawbacks for modelling stirred tanks, such as the large number of modelled revolutions required to obtain good statistical averaging for calculating turbulence quantities. Taking into consideration both accuracy and solution time, the SSG-RSM model was the least satisfactory model tested for predicting turbulent flow in a baffled stirred tank with a Rushton turbine.

In the second part of the work, experiments to determine suitable oxygen transfer rates for culturing cells were carried out in a stirred tank oxygenated using either a sparger to bubble air through the culture medium or a gas-permeable membrane. Results showed that the oxygen transfer rates for both methods of oxygenation were always above the minimum oxygen requirements for culturing animal cells commonly produced in industry, although the oxygen transfer rate for air-bubbling was at-least 10 times higher compared with using a gas-permeable membrane. These results pave the way for future experiments, in which animal cells would be cultured in the stirred tank using bubbling and (separately) a gas-permeable membrane for oxygenation so that the effect of rising and bursting bubbles on cell damage/death rates can be quantified. The effect of impeller agitation on cell damage/death would be quantified by using the gas permeable membrane for oxygenation (to remove the detrimental effects of bubbling), and changing the impeller speed to observe the effect of agitation intensity.

In the third and final part of this work, the turbulent flow in the stirred tank used in the oxygenation experiments was simulated using CFD. The SST turbulence model with curvature correction was used in these simulations, since it was found to be the most accurate model for predicting turbulence energy dissipation rate in a stirred tank. The predicted local maximum turbulence energy dissipation rate of 8.9×10^{1} m^2/s^3 at a rotational speed of 900 rpm was found to be substantially less than the value of 1.98×10^{5} m^2/s^3 quoted in the literature as a critical value above which cell damage/death becomes significant. However, the critical value for the turbulence energy dissipation rate quoted in the literature was determined in a single-pass flow device, whereas animal cells in a stirred tank experience frequent exposure to high turbulence energy dissipation rates (in the vicinity of the impeller) due to circulation within the stirred tank and long culture times. Future cell-culturing experiments carried out in the stirred tank of this work would aim to determine a more appropriate critical value for the turbulence energy dissipation rate in a stirred tank, above which cell damage/death becomes a problem.

1 Introduction

Animal cells are used extensively in *in vitro* cultivation for cell research and manufacture of biological products. The product may be the cells, cell components or metabolites which are produced naturally or by expression of recombinant DNA (Garcia-Briones & Chalmers, 1994). To achieve maximum yields, it is important to provide the cells with an *in vitro* environment as similar as possible to the natural cell environment. Such an environment can be produced within an aerated and stirred bioreactor. However, animal cells are sensitive to the fluid-mechanical forces associated with stirring and/or aeration via bubbling (Garcia-Briones & Chalmers, 1994). An understanding of the damage mechanisms caused by such forces is important for effective bioreactor design. Thus research into the shear sensitive nature of the cells could provide information that would allow one to define an appropriate environment in which the cells could be cultured at any scale.

In a bio-reactor, sufficient oxygen supply is necessary for animal cell survival. However, aeration by means of bubbling air can result in cell damage due to rising and bursting of bubbles (Tramper, Williams, Joustra, & Vlak, 1986). In addition, Yusuf Chisti (2001) found that animal cells are damaged by hydrodynamic stresses caused by agitation, such as produced by a stirrer, even in the absence of gas bubbles. Kunas and Papoursakis (1990) summarised that aeration via bubbling air and/or agitation are the two main fluid mechanical forces associated with cell damage. Cell damage due to aeration via bubbling air can be avoided by using gas-permeable membranes, as demonstrated by Kunas and Papoursakis (1990) and Schneider *et al.* (1995). One of the objectives of this study is to conduct oxygen mass transfer experiments in a stirred tank, in which aeration is provided either via bubbling or through use of gas-permeable membranes. No cells will be cultured in these preliminary experiments. Rather, suitable operating conditions will be found (for example, suitable air flow-rates for bubbling) so that the minimum oxygen transfer rate requirements for culturing cells in a stirred tank recommended in the literature are met. Future studies can then focus on separating the effects of animal cell damage due to bubbling and agitation by comparing cell death rates in a stirred tank with and without bubbling.

Scientists have used various experimental techniques to understand the shear effects and damage caused by aeration and agitation. However, experiments are not only costly and labour intensive, but also the parameters extracted are often specific to geometry and represent averages over the whole domain (Table 1-1). Thus, the results cannot be extrapolated to different vessel sizes and to other equipment designs. Computational Fluid Dynamics (CFD) is a relatively inexpensive method that can be used to investigate various flow parameters known to affect cell death rates. Through CFD, such flow parameters can be estimated locally throughout the flow domain. CFD could help not only to determine the relevant parameters of the flow field which govern hydrodynamic-related cell injury and their sensitivity to the geometry and operation of the equipment, but also to extrapolate results to different vessel sizes and to different equipment designs. Another aim of this study is to build a CFD model of a stirred tank to enable various hydrodynamic properties known to affect death rates of shear sensitive animal cells to be quantified and investigated.

1.1 Oxygen requirements in cells

The viability and growth of cells in sparged reactors depend, amongst other factors, on the bubble size and the bubble frequency, which can be controlled by the gas flow rate or the superficial gas velocity (Joshi, Elias, & Patole, 1996). Joshi *et al.* (1996), in agreement with Wu and Goosen (1995), suggested that the maximum cell damage occurs mainly in the region of bubble disengagement at the air-liquid interface. Various methods of oxygenation without the formation of bubbles have also been researched to avoid cell damage/death due to cell-bubble interactions, such as using gas–permeable membranes (Kunas & Papoutsakis, 1990; Schneider, *et al*., 1995). A gas permeable membrane is essentially a long coiled gas-permeable tube placed within the stirred tank, with oxygen or air flowing within the tube, which allows oxygen to diffuse through the permeable wall (membrane) of the tube and into the culture medium. This approach allows mixing and hence mass transfer rates to be enhanced through increased agitation to a higher intensity than can be achieved when oxygenating by bubbling, with good resultant cell growth rates and acceptable cell damage/death rates.

In this work, experimental oxygen mass transfer experiments will be conducted in a stirred-tank reactor using two different oxygenation methods, through bubbling and by

using a gas-permeable membrane. Appropriate operating conditions of the stirred tank when working with cells using these different oxygenation methods will be determined.

1.2 Parameters to characterize hydrodynamic stress

Various parameters that have been correlated with cell damage in a stirred tank include impeller speed, impeller tip velocity, integrated shear factor, time average shear rate and shear stress, specific power dissipation, and Kolmogorov eddy length scale, as shown in Table 1. However, there is little information available on how to use flow parameters that correlate well with cell damage in one particular system to predict cell damage in a different system. Garcia-Briones and Chalmers (1994) stated that cell damage should ideally be predicted by knowing the actual stresses that the cell experiences, determined from intrinsic cell mechanical properties and the resulting cell deformation. Should the cell deformation exceed a critical value, the disruption of the cell structure would be expected. They suggested that the parameter chosen to correlate with cell damage should be **1)** general in nature and not be dependent on the particular stirred-tank geometry and **2)** be local, that is, not be averaged throughout the flow domain. They proposed that two local intrinsic flow characteristics of general nature affect cell deformation: the local state of stress (proportional to actual stress that cells experience) and the vorticity of the suspending fluid.

Garcia-Briones and Chalmers (1994) rejected the Kolmogorov eddy scale as a basis for predicting cell damage, because essentially cell size becomes the only correlation parameter when this parameter is used, and therefore cell mechanical properties are neglected. Kunas and Papoutsakis (1990) suggested that, although Kolmogorov eddy length can be used as a predictor of cell damage, it does not provide any details of how cells are damaged by their interaction with these eddies or even prove that there is a direct cell-eddy interaction. Echoing this sentiment, Joshi *et al.* (1996) stated that it is very difficult to predict the relationship between the eddy size and its role in cell damage.

Mollet *et al.* (2007) suggested the use of turbulence energy dissipation rate, ε, as an ideal parameter to characterize the potential of hydrodynamic stresses to damage cells. The advantage of using turbulence energy dissipation rate, ε, is that it is intrinsic to any moving fluid and is a scalar value (Mollet, *et al*., 2007). Moreover, it accounts for both

shear and extensional components of three-dimensional flow. Depending on the system geometry and the flow regime, the turbulence energy dissipation rate, ε, can be determined experimentally or obtained via computer simulations (Mollet, *et al*., 2007).

Mavros (2001) presented a review of various experimental techniques for determining important parameters associated with turbulent flow in stirred tanks, including turbulence energy dissipation rate. According to Mavros (2001), laser Doppler velocimetry and particle image velocimetry are the most predominant techniques, having evolved into relatively easy-to-use techniques and providing considerable information about the three-dimensional flow generated by the impeller within a stirred tank. Zhang *et al.* (2006) listed the efforts of various scientists devoted to the description and understanding of the physicochemical phenomena that occur in stirred tanks. He reported on the early work of Cutter (1966), who used a hot-wire anemometry and photography to measure the mean and fluctuating velocities in stirred tanks. Wu and Patterson (1989) used laser Doppler velocimetry to investigate the flow in stirred tanks and presented the axial profiles of the mean velocity components and root-mean-square velocity fluctuations at various radial locations. Rutherford *et al.* (1996) has presented laser Doppler velocimetry results in the tank stirred by dual Rushton impellers. Bakker *et al.* (1996) and Sheng *et al.* (1998) have used particle image velocimetry to investigate the bulk flow around a pitched-blade turbine. More recently, Ducci and Yianneskis (2005) have attempted to determine turbulence energy dissipation rate, ε, through measurement by two-point LDA.

All the experimental techniques mentioned above have the disadvantage of being extremely complicated and labour intensive. In comparison, CFD is a relatively quick and cheap method for the determining flow parameters known to correlate well with cell damage in stirred tanks, such as turbulence energy dissipation rate. The ability of CFD for modelling stirred tank reactors has been aided by vastly increasing computing power and storage capacity with each passing year. CFD is more attractive and practical than experimental methods as a means of understanding the highly complex turbulent flow patterns that occur in a stirred tank reactor and the possible effect of this on cell damage. The key is that CFD models must first be validated by comparison with experimental data before they can be used with confidence for such means. In this project, a CFD approach to modelling turbulent flow in stirred tanks will be validated using well-known experimental data published in the literature.

Table 1-1: Various parameters used to correlate to cell death

Cells used	**Range of hydrodynamic Parameters**	**Important Observations**	**Reference**
Insect Cells, SF-21	210- 510 rev min^{-1} $\tau = 3$ N m^{-2} Cell death rate proportional to volumetric gas flow rate	"Viability of cells decreased at shear stresses of 1 N m^{-2}"	Tramper *et al.* (1986)
Hybridoma CRl-8018	60-900 rev min^{-1}, Cell death correlates to Kolmogorov eddy size similar to or smaller than the cell	"In absence of gas sparging, cells are damaged only at speed above 700 rev min^{-1}. No damage was seen at speeds less than 600 rev min^{-1}"	Kunas and Papoutsakis (1990)
Hybridoma HDP-1	100-440 rev min^{-1} Impeller tip speed 19-73.3 cm s^{-1}	"Death rate constant, increased sharply at impeller tip speeds above 40 cm s^{-1}"	Abu Reesh and Kargi (1989)
SF-9 and Hybridoma, serum containing, gas free	<0.7 impeller tip speed <350 W m^{-3} Power Inputs	"Damaging threshold values of impeller tip speed or specific Power inputs for some animal cells"	Chisti (2001)

1.3 Scope of the Project

The main aim of this project is to validate a Computational Fluid Dynamics approach for accurately determining important flow parameters known to affect the growth of shear sensitive cells in a stirred bioreactor. A secondary aim is to determine aeration rates suitable for cell culturing in a stirred tank when aeration is provided by either bubbling or through the use of a gas-permeable membrane.

The thesis can be summarized as follows. In Chapter 2, a CFD model of a stirred tank will be described and validated by comparison with the well-known published experimental results of Wu and Patterson (1989) and Ducci and Yianneskis (2005). In Chapter 3, oxygen transfer rates measured in a stirred tank reactor at various gas flow rates and impeller rotational speeds will be reported. Two modes of oxygenation will be investigated: bubbling and a gas-permeable membrane. This is essentially preliminary

work to determine appropriate aeration rates for culturing cells in the stirred tank reactor being investigated. Future work would involve experimentally culturing cells in this stirred tank reactor using either bubbling or a gas-permeable membrane for aeration. The same impeller speed would be used in both cases, and the cell death rates would be compared to determine the effect of cell-bubble interactions on the cell death rates. This would also allow the effect of cell death due to bubbling and agitation by stirring to be separated. In Chapter 4, the validated CFD model developed in Chapter 2 will be used as a starting point to model the stirred tank reactor used in the oxygenation experiments. Turbulence energy dissipation rate will be extracted from these CFD simulations. Future work would involve experimentally measuring cell death rates at various impeller rotational speeds within the stirred tank reactor and correlating the turbulence energy dissipation rate determined using CFD with the cell damage or death rates measured experimentally. The ultimate aim would be to use this information to ascertain appropriate operating conditions for culturing cells in stirred tank reactors of any scale.

2 Validation of the CFD Model

Stirred tanks are widely used in industry for dispersing gases or solids in liquids, crystallization, polymerization, and to perform chemical reactions and bio conversions. In the past, stirred tank design was confined to the use of empirical correlations because more detailed analysis of the flow fields by means of Computational Fluid Dynamics (CFD) was not reliable due to limitations on computer power and memory. As a result of these limited resources, CFD simulations of stirred tanks were restricted to coarse grids and steady-state predictions, or in the case of transient simulations, the use of large time steps that did not properly resolve the transient flow features. In addition, these limited resources also constrained the use of turbulence models to two-equation models, which assume an isotropic eddy viscosity, although the flow in the impeller region of the stirred tank has been demonstrated to be anisotropic (J. J. Derksen, Doelman, & Van den Akker, 1999; Escudié & Liné, 2006; Lee & Yianneskis, 1998). These issues have resulted in unsatisfactory agreement between experiment and CFD simulations (Hartmann *et al*., 2004; Jones, Harvey III, & Acharya, 2001; Montante, Lee, Brucato, & Yianneskis, 2001; Ng, Fentiman, Lee, & Yianneskis, 1998; Sheng, *et al*., 1998). However, advances in computer technology and mathematical models have enabled researchers to use finer computational grids and smaller time-steps, as well as more complex turbulence models (Delafosse, Liné, Morchain, & Guiraud, 2008). The present work aims to test the accuracy of CFD for predicting the turbulent flow field in a stirred tank using recently developed turbulence models and best practice numerical methods.

Another aspect of concern in CFD modelling of stirred tanks has been the definition of the kinetic energy of fluctuating motions. Wu and Patterson (1989) showed that this kinetic energy consists of two components, a random component and a periodic component, with the total kinetic energy being the sum of these two components. The random component is due to turbulent eddies, while the periodic component is due to non-random oscillations caused by the cyclic passage of the impeller blades. The periodic component appears in the turbulence energy spectrum as peaks at the impeller blade frequency and harmonics thereof. Montante *et al*. (2001), Hartmann *et al*. (2004), Murthy and Joshi (2008) and Delafosse *et al*. (2008) have separated these components in the modelling of stirred tanks. However, many other researchers have not made this distinction clear. The turbulence

kinetic energy predicted by the Reynolds-Averaged Navier-Stokes (RANS) based models, such as *k-ε*, *k-ω*, SST and Reynolds-stress models, corresponds to the random component of the kinetic energy of fluctuating motions (Montante, *et al*., 2001). This modelled turbulence kinetic energy comes about through Reynolds-averaging of the Navier-Stokes equations, which is carried out to avoid resolving unsteady turbulent eddies directly, thus reducing the computational effort. In the case of turbulence models that contain "LES content" for unsteady simulations, such as the SAS-SST (Menter & Egorov, 2005), large-scale turbulence is resolved directly to a certain extent, while the smaller-scale turbulence is dealt with through Reynolds-averaging. Thus, the predicted kinetic energy due to random fluctuations is the sum of the turbulence kinetic energy due to the directly-resolved large eddies and that coming about through Reynolds averaging. This is made more complex, because the periodic kinetic energy must first be extracted before the random component can be determined.

Transient simulations of stirred tanks have been well documented for the *k-ε* and LES models. Although the *k-ε* model is the most commonly used model for stirred tank simulations, its use of the Boussinesq approach of modelling Reynolds stresses using mean velocity gradients and an isotropic eddy viscosity means a limit is placed on the simulated development of anisotropic turbulence (Bakker, *et al*., 1996; Jahoda, Mostek, Kukuková, & Machon, 2007; Javed, Mahmud, & Zhu, 2006; Ng, *et al*., 1998; Yeoh, Papadakis, & Yianneskis, 2004; Zhang, *et al*., 2006). To overcome this limitation, many researchers have suggested using the Reynolds stress models (RSM), in which case each Reynolds stress is modelled with a separate transport equation, which eliminates the assumption of the isotropic eddy viscosity. However, both steady-state and transient results of the Reynolds stress model have shown an under-prediction of turbulence kinetic energy (Bakker, *et al*., 1996; Montante, *et al*., 2001; Murthy & Joshi, 2008; Sheng, *et al*., 1998). Another approach that can improve two-equation model predictions is the inclusion of a curvature correction term to sensitize the model to the effects of streamline curvature and system rotation (Smirnov & Menter, 2009). As far as the authors are aware, this approach has not been investigated for stirred-tank simulations.

Some researchers have ventured towards other turbulence models for simulating stirred tanks, such as the shear stress transport (SST) and scale adaptive simulation (SAS-SST) (Hartmann, *et al*., 2004; Honkanen, Vaittinen, Saarenrinne, & Korpijärvi, 2007). The SST

model is a hybrid model that combines the best features of the *k-ε* and *k-ω* models, switching from the *k-ω* model in the near-wall region to the *k-ε* model in the free stream using a smoothing function. The SST model has been shown to accurately predict flows with adverse pressure gradients and separation. However, it is unable to resolve any details of unsteady turbulent structures, which is often required (at least to some extent) to increase the accuracy of unsteady-flow predictions (Menter, 2009). The SAS-SST turbulence model is a recent development by Menter and Egorov (2005) to overcome this limitation. This model is formulated on the idea of capturing as much as possible of the turbulence field that an LES simulation would resolve but making use of the RANS capabilities near walls and regions of "steady" flow (Menter, 2009). Honkanen *et al.* (2007) have shown that the length and intensity of the trailing vortices that are generated off the impeller blades in a stirred tank are predicted well by the SAS-SST model, and are under-predicted by the SST model, which shows that the SST model over-estimates the dissipation rate of the turbulent structures. However, in their study, Honkanen *et al.* (2007) did not provide a detailed comparison between experimental data and simulated results of periodic and turbulence (or random) kinetic energy and turbulence energy dissipation rate obtained using the SST and SAS-SST.

This study section's focus is to conduct a detailed and comprehensive assessment of the ability of the *k-ε*, SST, RSM and SAS-SST turbulence models to predict important flow parameters associated with stirred tanks, such as the periodic and turbulence (random) kinetic energy, turbulence energy dissipation rate, turbulence length-scale, trailing vortices and power number. Care is taken to properly separate the random and periodic components of the kinetic energy of fluctuating motions. The experimental data of Wu and Patterson (1989) for a standard configuration system stirred by a Rushton turbine are used for validation. This data set is a standard used by many workers for validating simulations of stirred tanks (Brucato, Ciofalo, Grisafi, & Micale, 1998; Coroneo, Montante, Paglianti, & Magelli, 2010; Deglon & Meyer, 2006; J. Derksen & Van den Akker, 1999; Zadghaffari, Moghaddas, & Revstedt, 2010; Zhang, *et al*., 2006). The data of Wu and Patterson (1989) are supplemented with the experimental data of Ducci and Yianneskis (2005), also for a standard configuration tank stirred by a Rushton turbine. As will be explained in more detail below, Ducci and Yianneskis (2005) have shown that the experimental method used by Wu and Patterson (1989) results in a 40% underestimation

of the local maximum turbulence energy dissipation rate near the impeller, with the location of the maximum estimated to be too close to the impeller tip. They have obtained more accurate experimental data for the turbulence energy dissipation rate using a four-channel LDA and high spatial resolution to properly resolve the dissipative scales.

2.1 The Computational Model

2.1.1 Turbulence modelling

In this section, the various turbulence closures used in this study are described. The equations used for each model are those as coded in version 12.1 of ANSYS CFX (2009).

All of the models used in this study are derived from Reynolds-averaging of the underlying Navier-Stokes equations. This process introduces Reynolds stresses that have to be modelled to form a closed system of equations. The manner in which this is done impacts both the reliability of the modelled equations and the computational cost required to solve them.

In two-equation models, the Boussinesq hypothesis is used to model the unknown Reynolds stresses by assuming they can be approximated by the product of the mean strain rate multiplied by an isotropic turbulence viscosity. There are a variety of models that have been formulated but here we focus on just two of them. Firstly, the k-ε model, based on transport equations for the turbulence kinetic energy, k, and the turbulence energy dissipation rate, ε, is used. Whilst this model has known limitations, particularly its unsatisfactory performance in the near-wall region, it is still very widely used and also provides a good starting point to generate an initial flow field for more complicated models.

The k-ε model employs wall functions as the equations cannot be integrated to the wall. In order to address this problem, models in which the turbulence energy dissipation rate is replaced by the turbulence eddy frequency, ω, have been derived. These behave well near the wall and allow the detailed behaviour inside the boundary layer to be calculated. However, they perform poorly away from walls due to a problem with over-sensitivity to the free stream conditions. Menter (1994) blended the k-ε and k-ω models and added a turbulence production limiter in the calculation of the eddy viscosity to produce the now

widely used Shear Stress Transport (SST) model. It provides accurate predictions of the onset and the amount of flow separation under adverse pressure gradients (Menter, 1994).

A key failing of unsteady two equation models is that they cause excessive damping of turbulence and thus do not resolve any of the details of the turbulence directly (Menter, 2009). Menter and Egorov (2005) introduced the SAS-SST to overcome this deficiency. The SAS-SST model uses the von Karman length-scale (SAS stands for Scale Adaptive Simulation), which induces "LES-like" behavior in unsteady regions of the flow field. By adjusting the equations locally, damping of the resolved scales in the flow field is avoided (Menter, 2009; Menter & Egorov, 2005). Thus, unlike in the previous models, the grid length-scale enters directly into the conservation equations via the ratio of the grid length-scale to the von Karman length-scale.

Furthermore, another major drawback of eddy-viscosity RANS based models is the assumption of an isotropic turbulence viscosity, which limits the development of anisotropy in the Reynolds stresses. Reynolds stress models (RSM), which solve transport equations for each of the Reynolds stresses, remove this assumption. The model is much more computationally intensive than two-equation models and suffers from poor convergence behaviour (Aubin, Fletcher, & Xuereb, 2004). Just as there are many variants of the two equations models, there are a large number of Reynolds stress models that differ in their closure relationships, especially for the pressure-strain term. Here the variant of the model developed by Speziale, Sarkar and Gatski (1991), known as the SSG-RSM, is used. It is known to perform well in the simulations of strongly rotating flows, in, for example, cyclones.

A key limitation of two-equation models is their insensitivity to streamline curvature and rotation, which is the main motivation for the use of Reynolds stress models. Recently, a modification to the SST model has been developed by Smirnov and Menter (2009) based on the work of Spalart and Shur (1997). This has shown considerable benefit in applications where highly swirling flows have been modelled, but to our knowledge it has not yet been applied to the simulation of stirred tanks.

2.1.2 Description of the Test Case

A standard tank and Rushton turbine configuration was employed experimentally by Wu and Patterson (1989). The tank has a diameter and height of 270 mm with four equally spaced baffles of width one-tenth of the tank diameter. The impeller has a diameter of 93 mm with six blades and is located at one-third of the tank diameter from the base of the tank. The blades have a width and height of one-quarter and one-fifth of the impeller diameter, respectively. Water at 25 ^{o}C was used as the working fluid and the impeller rotational speed was 200 rpm, which corresponds to a Reynolds number of 28,830.

2.1.3 The Computational Mesh and Time-steps

Simulations were carried out using the sliding mesh technique with the impeller swept region as the inner rotating zone and rest of the tank, including the baffles, as the stationary zone. Only half of the geometry was modelled to reduce computational effort, which was possible due to the symmetry of a six-blade impeller and four baffles. The thicknesses of the impeller blades, impeller disc and baffles, which Wu and Patterson (1989) did not specify in their paper, were assumed to be zero in order to reduce the mesh complexity. Rutherford *et al.* (1996) have shown experimentally that the thickness of the impeller blades significantly influences the power number, mean velocities and turbulence levels. They measured a reduction in the impeller power number of 33 % with an increase in the ratio of blade thickness to impeller diameter from 0.0082 to 0.0337, with the impeller diameter remaining constant. Delafosse *et al.* (2008) showed a similar influence of the impeller thickness on the power number after comparing the power number of 5.5 measured by Escudié and Liné (2003) for a blade thickness to impeller diameter ratio of 0.0133 with the power number of 5 measured by Ducci and Yianneskis (2005) for a blade thickness to impeller diameter ratio of 0.03, both cases using an impeller of the same diameter.

In addition to the effect on power number, blade thickness also affects the mean and fluctuating velocities, mostly around the centre of the discharge stream of the impeller (at the impeller disk elevation). Rutherford *et al.* (1996) observed experimentally an increase in the maxima of the radial velocity of 26% and 11% at dimensionless radial distances r_R from the impeller axis of 1.048 and 1.752, respectively, as the blade thickness to impeller

diameter ratio decreased from 0.0337 to 0.0082. Moreover, they observed an increase in the maxima of the radial fluctuating velocity of 15% and 25% at dimensionless radial distances r_R of 1.048 and 1.752, respectively, as the blade thickness to impeller diameter ratio decreased from 0.0337 to 0.0082. CFD simulations of blades with a given thickness are often avoided because the thickness of the blade cannot be meshed sufficiently well while having a mesh that is practical from a computational point of view. Any differences between the prediction and experimental data in this paper may be due to the neglect of the impeller thickness in the simulations, as well as weaknesses in the turbulence models tested.

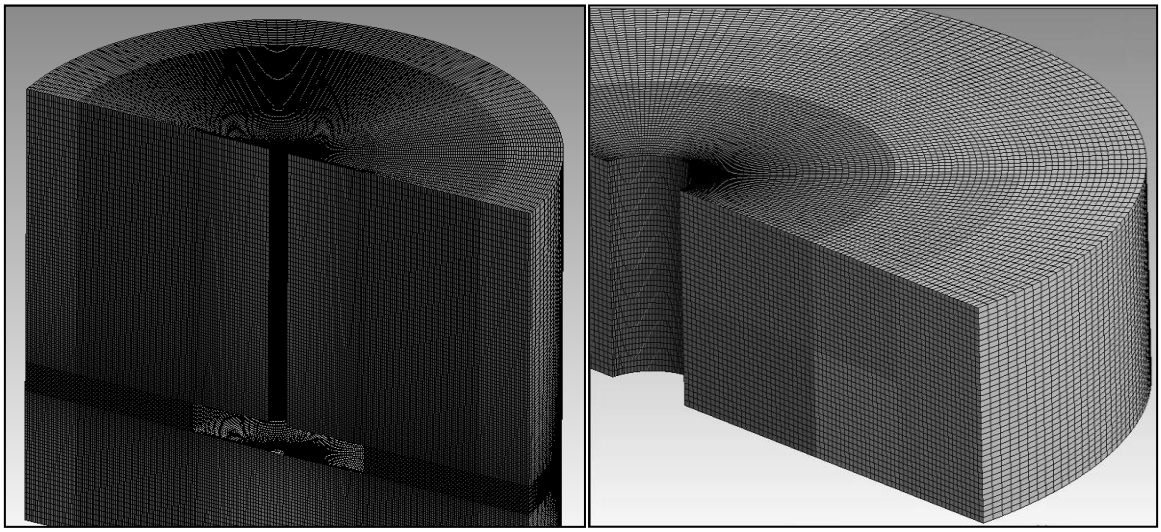

Figure 2-1: Views of the 2.138×106 node mesh for the tank and impeller zones.

The sliding interface was located at a radius corresponding to the tip of the impeller. No discontinuities in velocity, pressure, turbulence kinetic energy or turbulence energy dissipation rate were observed across the sliding interface with the mesh eventually adopted in the simulations (Figure 2-1), which indicates a good resolution of the mesh across the interface. Grid independence was tested with the SST turbulence model. In this case, the average percentage difference in the solution between meshes containing 1.644 and 2.138 million nodes for the mean total kinetic energy of fluctuating motions and mean turbulence energy dissipation rate was 7.2% and 3.7%, respectively, over the region examined (shown in Figures 2b and 2c). Moreover, the average percentage difference in the solution between these meshes for the power number based on torque (defined below) was only 1.5%. Further mesh refinement from 2.138 to 3.127 million nodes had very little

effect on the numerical solution for the mean total kinetic energy of fluctuating motions, mean turbulence energy dissipation rate and power number.

For the SAS-SST predictions, the average percentage difference between the meshes containing 1.644 and 2.138 million nodes for mean total kinetic energy of fluctuating motions and mean turbulence energy dissipation rate was 6.1% and 11.3%, respectively, over the region examined (shown in Figure 2-2d for turbulence energy dissipation rate). The value of 11.3% for the turbulence energy dissipation rate was considered to be too high to regard the SAS-SST predictions as being grid independent. For this turbulence model, a grid independent solution is more difficult to achieve, especially in the turbulence quantities, because further refinement of the mesh will result in smaller turbulent fluctuations (or eddies) being resolved. In this work, a mesh containing 2.138 million nodes, shown in Figure 2-1, was adopted for all of the turbulence models tested. Refining the mesh further to resolve even finer turbulent structures and obtain more accurate solutions for the SAS-SST was found to be prohibitively expensive computationally.

Figure 2-2 shows that little improvements in accuracy can be gained by moving from one degree resolution for the rotating impeller (equivalent to 8.3×10^{-4} s per time-step) to a 0.5 degree resolution using the same mesh (containing 1.027 million nodes) and the SST model. In this comparison, the average percentage error for both the mean total kinetic energy of fluctuating motions and the mean turbulence energy dissipation rate was about 0.4 % and 0.3%, respectively. For the SAS-SST model prediction with a mesh containing 1.027 million nodes and for 20 simulated revolutions, the average percentage difference in solutions for a time-step of 1 degree and 0.5 degree resolution for both the mean total kinetic energy of fluctuating motions and mean turbulence energy dissipation rate was about 2.0% and 6.4%, respectively, over the region examined. As with mesh refinement, further time-step refinement would result in better resolution of turbulence when using the SAS-SST model. However, such refinement is constrained by the computational effort that can be afforded.

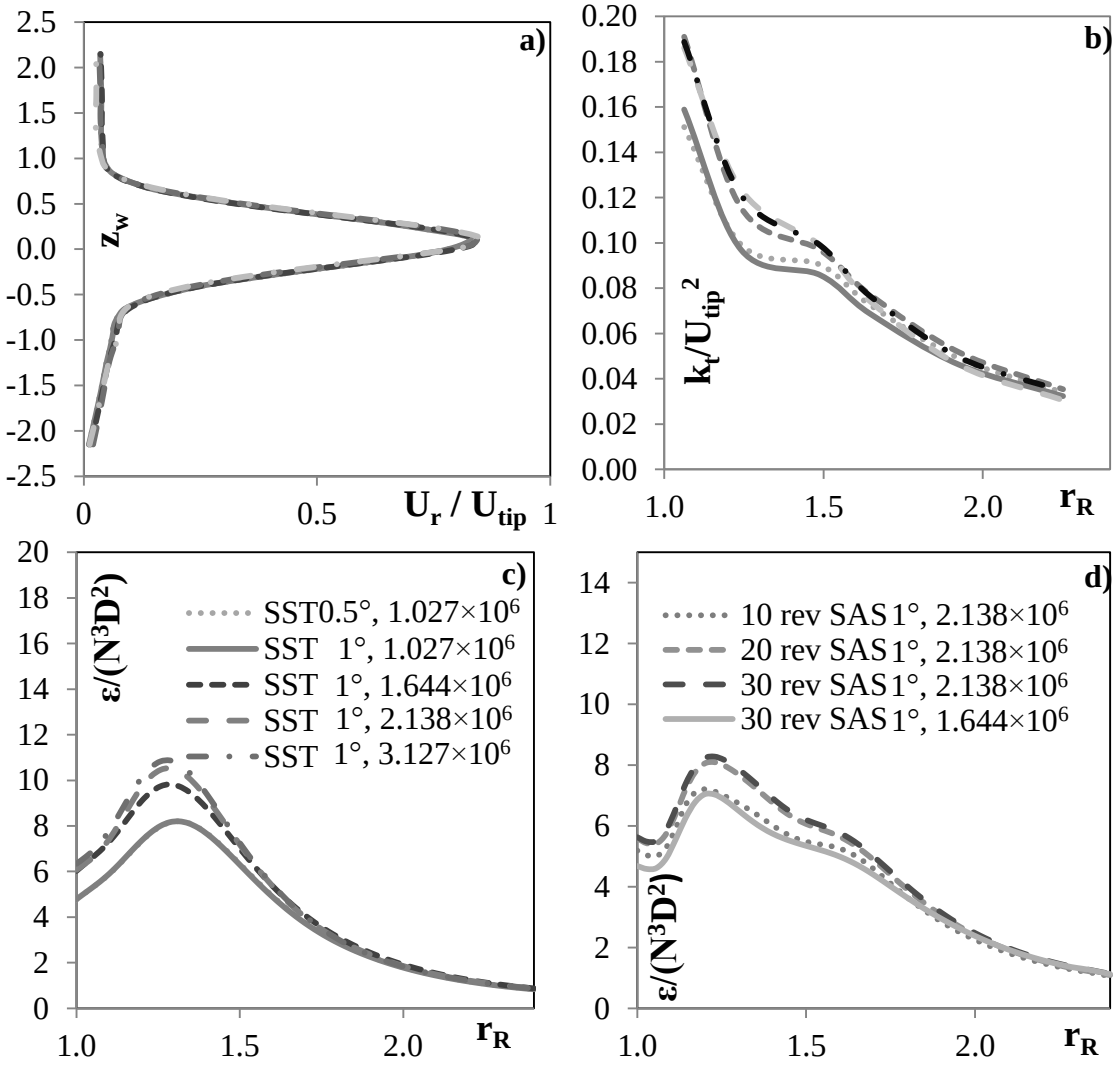

Figure 2-2. Grid and time-step independence check. (a) mean radial velocity at a dimensionless radial distance r_R of 1.07 from the impeller axis, (b) total kinetic energy of fluctuating motions and (c) turbulence energy dissipation rate for the SST turbulence model, and (d) turbulence energy dissipation rate for the SAS-SST turbulence model at the impeller disk elevation. The legend for Figure 2-2c applies to Figures 2-2a and 2-2b.

Only one revolution of data was collected for the *k-ε*, SST, and SSG-RSM models since repeat revolutions produced repeat data. In the SAS-SST, data representing a sufficient number of revolutions is required to ensure good statistical averages (Frank, Prasser, Menter, & Lifante, 2010). In this case, data was collected for 30 revolutions equivalent to around 9 seconds of real time. Figure 2-2d shows that 20 revolutions suffice to achieve time-averaged turbulence quantities that are independent of the number of further simulated revolutions.

Table 2-1 shows a comparison of various mesh sizes and time-steps used in recent studies. It can be seen that some researchers have used coarser meshes and longer time-steps than used in this work, perhaps due to limitations in computer power available but at the expense of a certain degree of accuracy.

Table 2-1: Mesh size and time-step used by various authors for transient simulations of flow in stirred tanks.

Author	Modelled tank geometry	Mesh size: In millions	Time-step: resolution in degrees
(Ng, *et al*., 1998)	Half	0.239 (cells)	1
(Montante, *et al*., 2001)	Half	0.080	4
(Hartmann, *et al*., 2004)	Full	0.242 (nodes)	4
(Yeoh, *et al*., 2004)	Full	0.49 (cells)	1.67
(Bakker & Oshinowo, 2004)	Full	0.763 (cells)	6
(Zhang, *et al*., 2006)	Not specified	1.728 (cells)	2.4
(Honkanen, *et al*., 2007)	Full	0.542 (nodes)	2.5
(Jahoda, *et al*., 2007)	Full	0.615	1.8
(Murthy & Joshi, 2008)	Not specified	0.575	Initially 0.16; gradually increased to 1.6
(Delafosse, *et al*., 2008)	Full	1 (cells)	0.5
(Coroneo, *et al*., 2010)	Full	6.6 (cells)	3.75
Present Study	Half	2.138 (nodes)	1

2.1.4 Computational Aspects

The advection terms were modelled using the high resolution scheme for all equations and the second order backward Euler scheme was used for the transient terms. The convergence criteria used for the continuity, momentum and turbulence quantities was an

RMS scaled residual of 10^{-5}. This was achieved in a maximum of 10 iterations per time-step for all the turbulence models presented in this study. Double precision arithmetic was used in all simulations. In these simulations, an un-converged steady-state simulation was used as the initial guess for the transient simulations. Collection of transient data was started only after a pseudo-steady state was achieved for all turbulence models.

The simulations have been performed using eight 1.9 GHz parallel processors each with 2 GB of memory. No significant computing time difference was observed between the *k-ε*, SST, SST-CC and SAS-SST models, with the simulation of one revolution with one degree resolution in time-step and with a mesh having 2.138 million nodes being achieved in about 55 hours compared with 90 hours for the SSG-RSM model.

2.1.5 Data Post Processing

Kinetic Energy of Fluctuating Motions for the *k-ε*, SST and RSM Models

In the case of the RANS turbulence models (*k-ε*, SST and RSM models), the instantaneous velocity for a given point in the tank can be defined as the sum of the mean velocity, the periodic velocity and a random velocity, as defined in Equation (2-1) below:

$$u_{ins} = \bar{u} + u_p + u_r \tag{2-1}$$

Only the mean and periodic velocity components can be resolved directly in RANS simulations, provided these simulations are transient. In this case, the velocity at a point will oscillate in a regular manner around the mean due to the cyclic passage of the impeller blades. For example, with six blades, one revolution of the impeller will result in six oscillations. The transient velocity field in RANS simulations, u_i, can be decomposed as follows:

$$u_i = \bar{u} + u_p \tag{2-2}$$

The time-averaged periodic velocity component in a given direction can be extracted as follows:

$$\overline{u_p u_p} = \frac{1}{n}\sum_{i=1}^{n}(u_i - \bar{u})^2 \tag{2-3}$$

where *n* is the number of time-steps over which the time-averaging takes place. The components in the other two orthogonal directions are extracted in the same manner. The periodic kinetic energy is then given by

$$k_p = \frac{1}{2}(\overline{u_P u_P} + \overline{v_P v_P} + \overline{w_P w_P}) \tag{2-4}$$

The random velocity component comes from RANS modelling through the turbulence kinetic energy (k_r). Thus, the total kinetic energy of fluctuating motions is given by

$$k_t = k_r + k_p \tag{2-5}$$

Kinetic Energy of Fluctuating Motions for the SAS-SST model

In the case of the SAS-SST model, the instantaneous velocity can also be described by Equation (2-1). However, the random velocity component, u_r, now becomes the sum of a random velocity due to the large eddies, $u_{le\text{-}r}$, which are resolved directly by the SAS-SST model and the random velocity due to the smaller eddies, $u_{se\text{-}r}$, which come from the RANS content of the model through the turbulence kinetic energy (*k*):

$$u_{ins} = \bar{u} + u_p + u_{le-r} + u_{se-r} \tag{2-6}$$

For SAS-SST simulations, the transient velocity at a point is resolved as follows:

$$u_i = \bar{u} + u' \tag{2-7}$$

where $u' = u_p + u_{le-r}$, which implies that any simulated fluctuations are caused by periodicity and large-eddies. The time-averaged component in each direction can be extracted separately,

$$\overline{u'u'} = \frac{1}{n}\sum_{i=1}^{n}(u_i - \bar{u})^2 \tag{2-8}$$

where *n* is the number of time steps over which the time-averaging takes place. The kinetic energy due to these fluctuations (periodic plus the large-eddy) is given by

$$k_{p+le-r} = \frac{1}{2}\left(\overline{u'u'} + \overline{v'v'} + \overline{w'w'}\right) \tag{2-9}$$

The total kinetic energy of fluctuating motions is therefore the sum of the kinetic energy due to the periodic and large-eddy fluctuations and kinetic energy due to the small-eddy fluctuations (calculated as the turbulence kinetic energy, *k*, from the SAS-SST model):

$$k_t = k_{p+le-r} + k \tag{2-10}$$

The periodic and large-eddy fluctuations are separated by effectively averaging out the fluctuations due to the large eddies. One impeller rotation is resolved using m_{total} angular positions. For example, for a 1 degree resolution, there are 360 angular positions before the impeller completes a full cycle and returns to its initial position. For a given repeat angular position of the impeller *m*, the velocity at a point can be averaged over a number of full turns:

$$\tilde{u}_m = \frac{1}{n_{TS}} \sum_{j=1}^{n_{TS}} u_{j,m} \tag{2-11}$$

where $u_{j,m}$ is the transient velocity at a point in the tank when the impeller has an angular position corresponding to *m*, and n_{TS} is the number of full turns of the impeller for which data are available. Clearly, the more full-impeller turns that have been simulated the better the average. Equation (2-11) can be used to calculate the periodic fluctuation (due to the cyclic passage of the impeller blades) once the effect of the large eddy fluctuations have been averaged out. The effect of this averaging can be seen clearly in Figure 2-3. Thus, the time-averaged periodic velocity components in each direction can be derived from the averaged periodic fluctuations over a full turn, such as shown in Figure 2-3, using Equation (2-3). The periodic kinetic energy is then given by

$$k_p = \frac{1}{2}(\overline{u_P u_P} + \overline{v_P v_P} + \overline{w_P w_P}) \tag{2-12}$$

The random component of the total kinetic energy can now be extracted as follows:

$$k_r = k_t - k_p = k_{p+le-r} + k - k_p \tag{2-13}$$

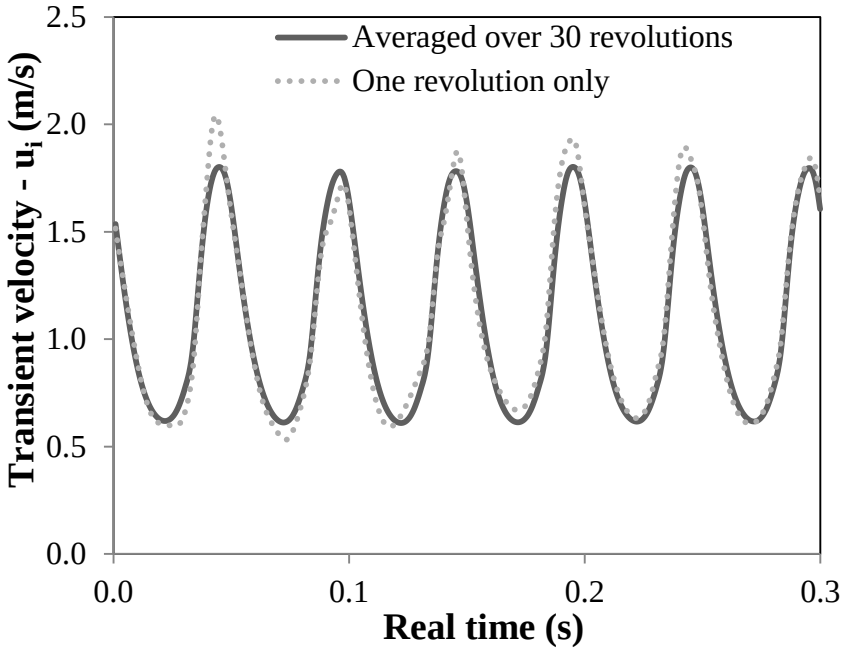

Figure 2-3: Effect of averaging on the periodic velocity calculated using the SAS-SST turbulence model with 1° time-step and a mesh with 2.138×10^6 nodes at a dimensionless radial distance r_R of 1.07 from the impeller axis at the axial height of the impeller disk.

Calculation of the Power Number

The power number can be obtained in two different ways from the numerical simulations: (1) using the torque applied on the impeller (Equation 2-14) and by integrating the turbulence energy dissipation rate ε over the tank volume (Equation 2-15), as follows

$$N_{P\tau} = 2\pi N\tau/\rho N^3 D^5 \tag{2-14}$$

and

$$N_{P\varepsilon} = \int \rho\varepsilon \mathrm{d}V \,/\rho N^3 D^5 \tag{2-15}$$

where N is the rotational speed in rev/s, τ is the torque applied on the impeller, ρ is the fluid density and D is the diameter of the impeller.

Calculation of the Turbulence Length-scale

The turbulence length-scales used in this study are given by Equation (2-16) for the *k-ε* and SSG-RSM model and by Equation (2-17) for the SST and SAS-SST models.

$$l = C_\mu^{3/4}.k^{3/2}/\varepsilon \tag{2-16}$$

$$l = \sqrt{k}/\left(C_{\mu}^{1/4}.\omega\right) \quad (2\text{-}17)$$

The constant C_{μ} takes a value of 0.09.

2.2 Results and Discussion

2.2.1 Mean Velocity Field

Figures 2-4a and 2-4b show that all of the turbulence models, except for the *k*-*ε* model, slightly over-predict the maxima of the mean radial and tangential velocity profiles at a dimensionless radial distance r_R of 1.07 from the centre of rotation. In addition, all models slightly over-predict the magnitude of the mean axial velocity below and above the blades of the impeller at this same radial location (Figure 2-4c). Figures 2-4d and 2-4e show that the SAS-SST model predicts the decay of the mean tangential and axial velocities radially away from the impeller reasonably well, although the mean radial velocity decays too slowly (Figure 2-4f). Similar comparisons as seen in Figures 2-4d, 2-4e and 2-4f have been conducted between experiment and prediction for all other turbulence models tested; however, for the sake of brevity, figures showing these comparisons are not provided here. In general, all turbulence models tested modelled the decay of the mean tangential and axial velocity radially away from the impeller reasonably well, but they under-predicted the decay of mean radial velocity. Nevertheless, all these models at least qualitatively predict the radial jet-like flow away from the impeller and the entrainment of fluid into the jet from the bulk flow, which causes the jet to broaden and decrease in speed. Finally, using curvature correction with the SST turbulence model did not appreciably change the mean velocity predictions compared with using the SST turbulence model alone.

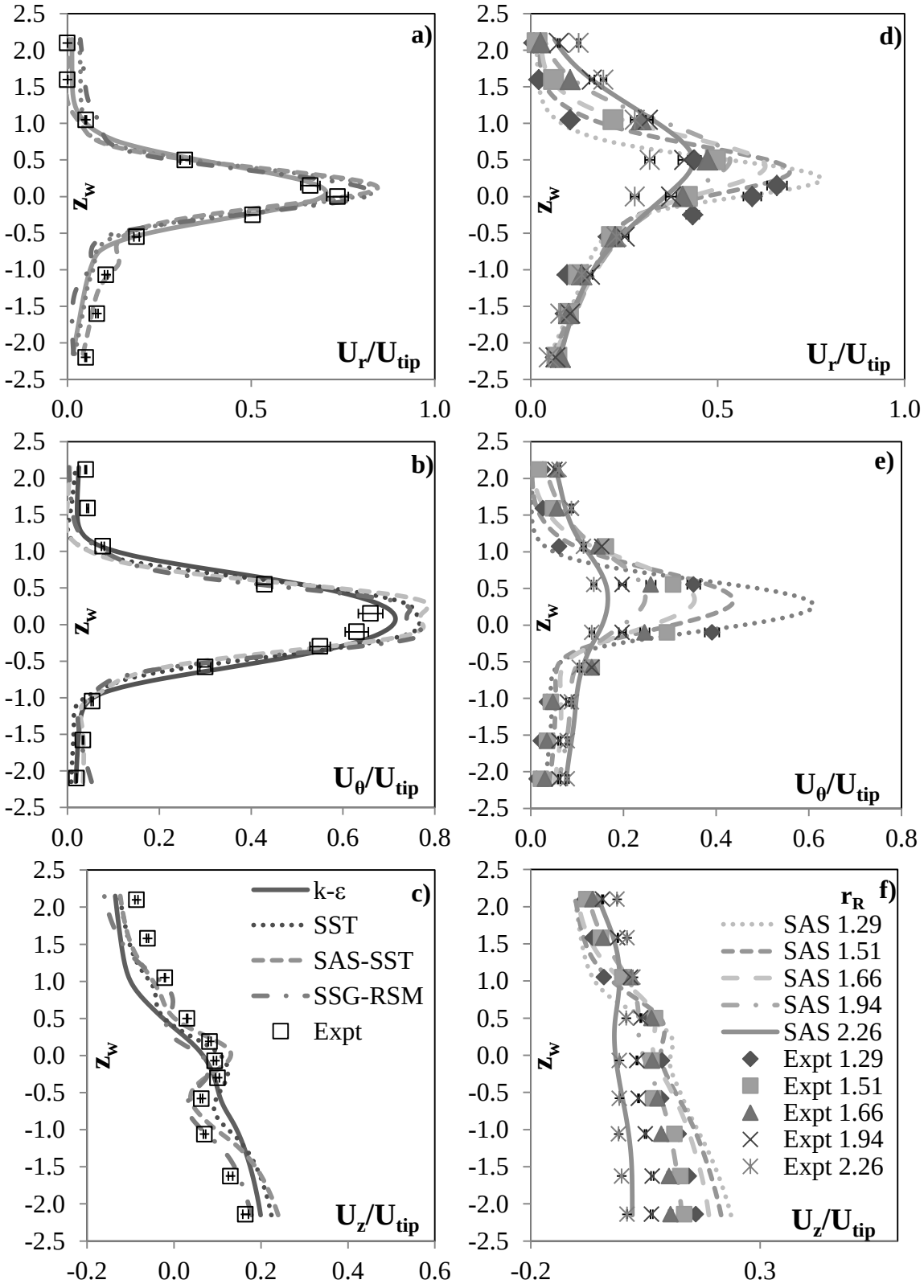

Figure 2-4. Mean radial, tangential and axial velocity profiles for different turbulence models at a dimensionless radial distance r_R of 1.07 from the impeller axis (a, b and c) and for the SAS-SST model at various radial locations (d, e, and f). The legend for Figure 2-4c applies to Figures 2-4a and 2-4b. The legend for Figure 2-4f applies to Figures 2-4d and 2-4e.

2.2.2 Kinetic Energy of Fluctuating Motions

Figures 2-5a, 2-5b and 2-5c present axial profiles of the periodic, random and total components of the kinetic energy of the fluctuating motions at a dimensionless radial distance r_R of 1.07 from the centre of rotation. All of the turbulence models, except for the *k-ε* model, over-predict the total kinetic energy of fluctuating motions. This over-prediction of the total kinetic energy, which only occurs in the vicinity of the impeller (Figure 2-5c), is directly related to the over-prediction of the periodic kinetic energy (Figure 2-5a). Away from the impeller, the agreement is better for all the turbulence models, except for the SSG-RSM model, as shown in Figures 2-5d and 2-5f. The *k-ε* model predicts the random, periodic and total components of the kinetic energy reasonably well away from the impeller. However, closer to the impeller, it severely under-predicts the periodic component and over-predicts the random component, which Delafosse *et al.* (2008) also found. Conversely, the SSG-RSM model severely over-predicts the periodic kinetic energy and under-predicts the turbulence (or random) kinetic energy. Murthy and Joshi (2008) have found a similar under-prediction of the turbulence (random) kinetic energy for the SSG-RSM.

None of the turbulence models are able to properly predict the peaks and local minimum in the turbulence (random) kinetic energy profile in the axial direction, as shown in Figure 2-5b. These peaks and local minimum are predicted only weakly by the SST and SAS-SST model and not at all by the SSG-RSM, SST-CC and *k-ε* models. Wu and Patterson (1989) state that the peaks correspond to the location of a pair of vortices, one vortex above and one vortex below the disk of the impeller, that originate from behind each blade and trail out into the bulk of the flow. Such trailing vortices, which will be visualized later in this paper, are predicted by all turbulence models tested.

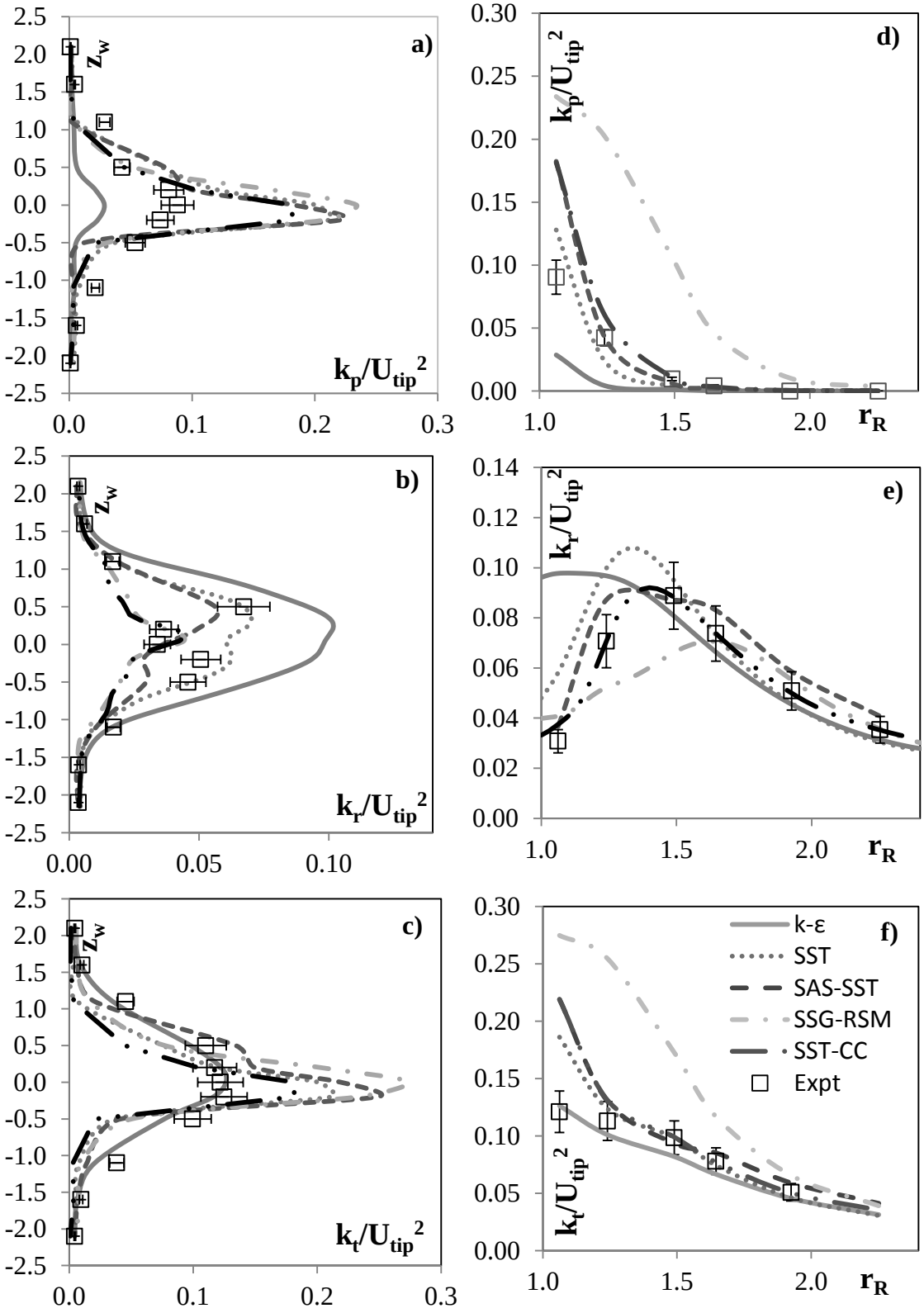

Figure 2-5: Comparison of different turbulence models for (a) periodic, (b) random and (c) total kinetic energy of fluctuating motions at a dimensionless radial distance r_R of 1.07 from the impeller axis and for radial profiles of (d) periodic, (e) random, and (f) total kinetic energy of fluctuating motions at the impeller disk elevation. The legend for Figure 2-5f applies to Figures 2-5a, 2-5b, 2-5c, 2-5d and 2-5e.

Regarding the turbulence (random) kinetic energy profile in the radial direction shown in Figure 2-5e, the SST, SST-CC and SAS-SST turbulence models predict the maximum at a dimensionless radial distance r_R of about 1.4 in agreement with the experimental results. The *k*-ε model predicts the maximum at the impeller tip, while the SSG-RSM model predicts the maximum at a dimensionless radial distance r_R of 1.6. Of all the turbulence models tested, the SST-CC predicts the periodic, random and total kinetic energy of fluctuating motions most satisfactorily. These predictions mirror the experimental observations of Wu and Patterson (1989), who found that periodic fluctuations dominate the turbulence field close to the impeller, as can be seen by the high values of k_p compared with k_r in this region, but decay rapidly away from the impeller in the radial direction. Meanwhile, the random turbulent fluctuations developed in the near impeller region, dominate at a dimensionless radial distance r_R of 1.4 and then decay further away.

2.2.3 Turbulence Energy Dissipation Rate

Figures 2-6 and 2-7 present the turbulence energy dissipation rate predictions of the different turbulence models tested in this paper. For comparison, two sets of experimental data are presented, the first by Wu and Patterson (1989) and the second by Ducci and Yianneskis (2005). The experimental turbulence energy dissipation rate determined by Wu and Patterson (1989) was calculated from the turbulence (random) kinetic energy by a fitted correlation rather than being measured directly. Ducci and Yianneskis (2005) have shown that this "dimensional" method tends to underestimate the local maximum turbulence energy dissipation rate near the impeller by about 40%. In addition, the location of this maximum is found to be too close to the impeller using this method. Ducci and Yianneskis (2005) measured ε directly and more accurately using a four-channel laser-Doppler anemometer (LDA) and a fine spatial resolution to properly resolve the dissipative scales. They found that the turbulence energy dissipation rate normalized with N^3D^2 was approximately constant between Reynolds numbers of 20,000 and 40,000. Given that the same standard tank configuration and Rushton turbine were used by both Wu and Patterson (1989) and Ducci and Yianneskis (2005), and that the Reynolds number in the experiments of Wu and Patterson (1989) was 28,830, then a direct comparison of the predictions of the turbulence models presented in this paper with the experimental data of Ducci and Yianneskis (2005) is possible.

Note that in the paper of Wu and Patterson (1989), profiles of turbulence energy dissipation rate normalized with an average turbulence energy dissipation rate ε_{avg} are presented. In order to estimate ε_{avg} so that these profiles could be re-dimensionalised here, Equation (15) was used with a power number of 5, which Wu and Patterson (1989) assumed on the basis of measurements conducted by Bates *et al.* (1963). Another point is that Ducci and Yianneskis (2005) only provide one axial profile of turbulence energy dissipation rate at a radial location of 1.35 r_R. This position lies between the two radial locations (at 1.29 r_R and 1.5 r_R) of the turbulence energy dissipation rate axial profiles measured by Wu and Patterson (1989). In order to allow a good comparison, the axial ε profile of Ducci and Yianneskis (2005) at 1.35 r_R is overlaid on both the axial ε profiles of Wu and Patterson (1989). An axial profile of turbulence energy dissipation rate at 1.07 r_R is shown in Figure 7c, which will be discussed in relation to predicted power numbers further below.

Figure 2-6 shows that the *k*-ε model predicts the location of maximum turbulence energy dissipation rate to be near the impeller tip, in agreement with the *k*-ε model predictions of Delafosse *et al.* (2008). This does not agree with the experimental results, which suggest that the location of the maximum is at a dimensionless radial distance r_R of around 1.4. The SST model is able to predict the appearance of a maximum and its magnitude, although its location does not align with that of the experimental data. Curvature correction helps to improve this prediction. Indeed, the SST-CC model accurately predicts both the increase in turbulence energy dissipation rate radially away from the impeller tip in the near-impeller region, where turbulence is developing, and the decrease of the turbulence energy dissipation rate further away from the impeller, where turbulence decays.

Neither the location of the maximum nor its magnitude is predicted well by the SAS-SST and SSG-RSM models, as shown in Figure 2-6. The SSG-RSM is the least accurate model tested. Given that this model also requires more than one-and-a-half times the computational time of the *k*-ε and the SST-based models, it would be a poor choice of turbulence model for predicting flow in baffled stirred tanks. Unfortunately, as indicated by the numerical-solution verification check detailed above (illustrated in Figure 2-2d), further refinement of the mesh is required before any conclusions can be drawn about the accuracy of the SAS-SST turbulence model for predicting the turbulence energy

dissipation rate. Such refinement proved to be impractical from a computational perspective in this work due to the significant number of impeller revolutions required to gain good statistical averages of the turbulence quantities and the prohibitively long time needed to achieve this.

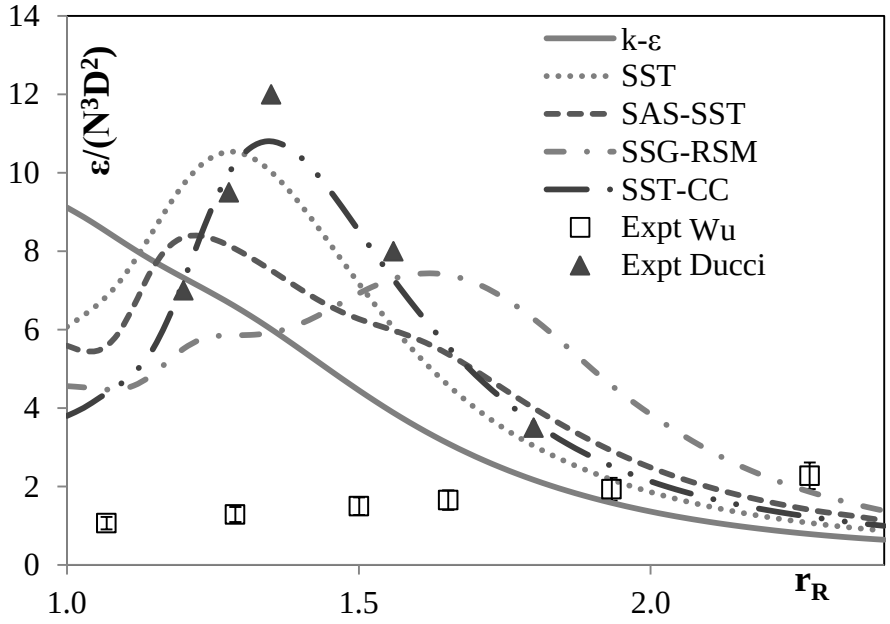

Figure 2-6: A comparison of the radial profile of normalized turbulence energy dissipation rate at the impeller disk elevation for various turbulence models.

A comparison with the data of Ducci and Yianneskis (2005) indicates that all turbulence models under-estimate the width of the turbulence energy dissipation rate profile in the axial direction (Figure 2-7). Thus, it is reasonable to assume that, in general, the turbulence models under-predict the volume-integral of the turbulence energy dissipation rate throughout the tank. As will be discussed below, this has repercussions for the accurate prediction of power number based on the volume-integral of the turbulence energy dissipation rate (Equation 2-15). Note that the experimental data of Ducci and Yianneskis (2005) at 1.35 r_R are more appropriately compared with the predictions shown in Figure 2-7a, which apply at a location of 1.29 r_R. Further away radially, the predicted turbulence energy dissipation rates decrease and become even lower relative to the experiment measurements at 1.35 r_R, which further highlights the under-estimation of the turbulence energy dissipation rate by all turbulence models tested.

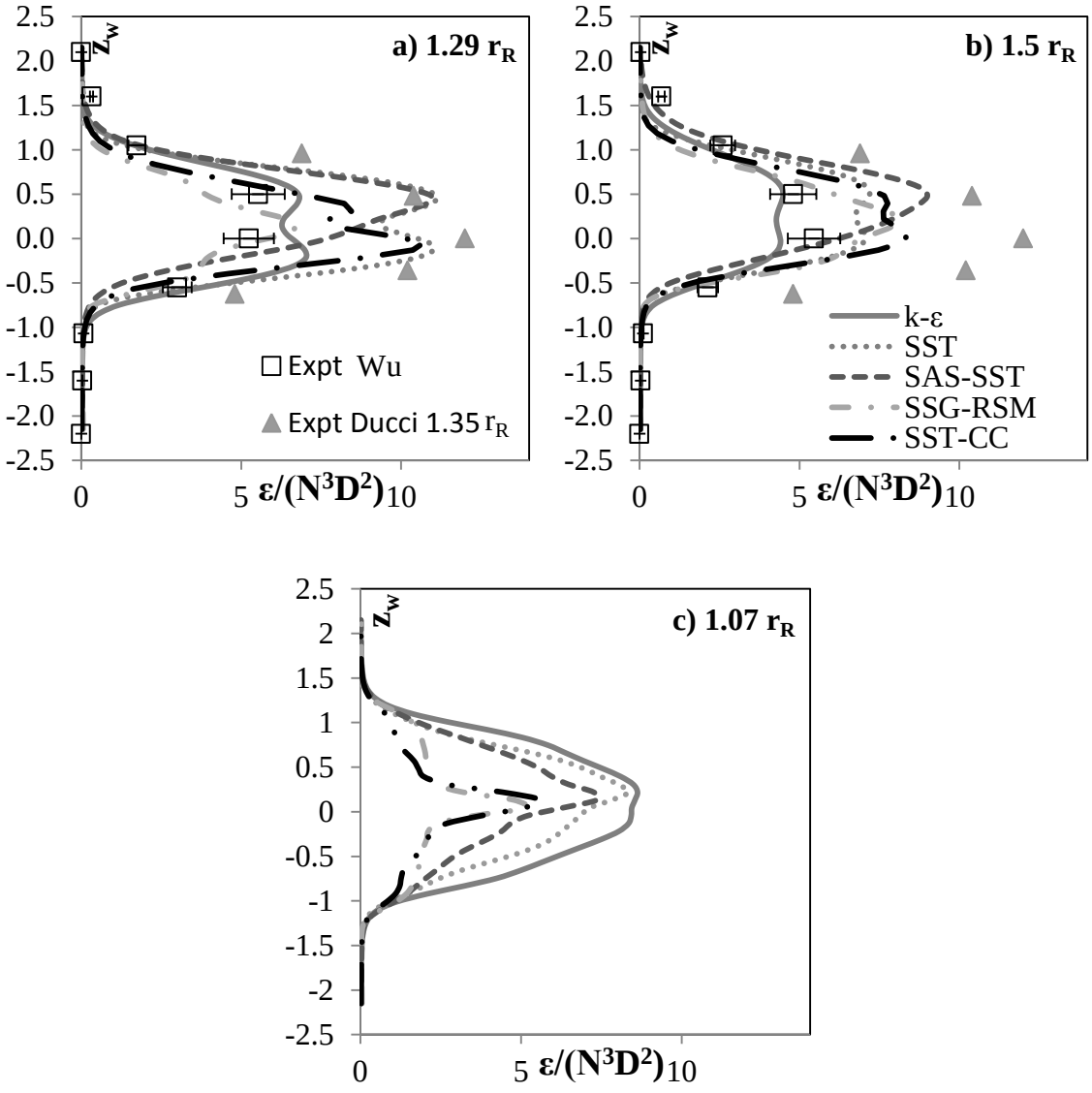

Figure 2-7: Axial profiles of normalized turbulence energy dissipation rate at various radial locations for different turbulence models. The legends for Figures 2-7a and 2-7b apply to Figures 2-7a, 2-7b and 2-7c.

2.2.4 Trailing Vortices and Turbulence Length-scale

The vortical structures in a flow can be visualized in a number of different ways. Here we have used the swirling strength, based on the computation of the eigenvalues of the velocity gradient tensor. A threshold value of 0.1 was found to be a good compromise between missing structures if the value was too high and masking the structures if the value was too low.

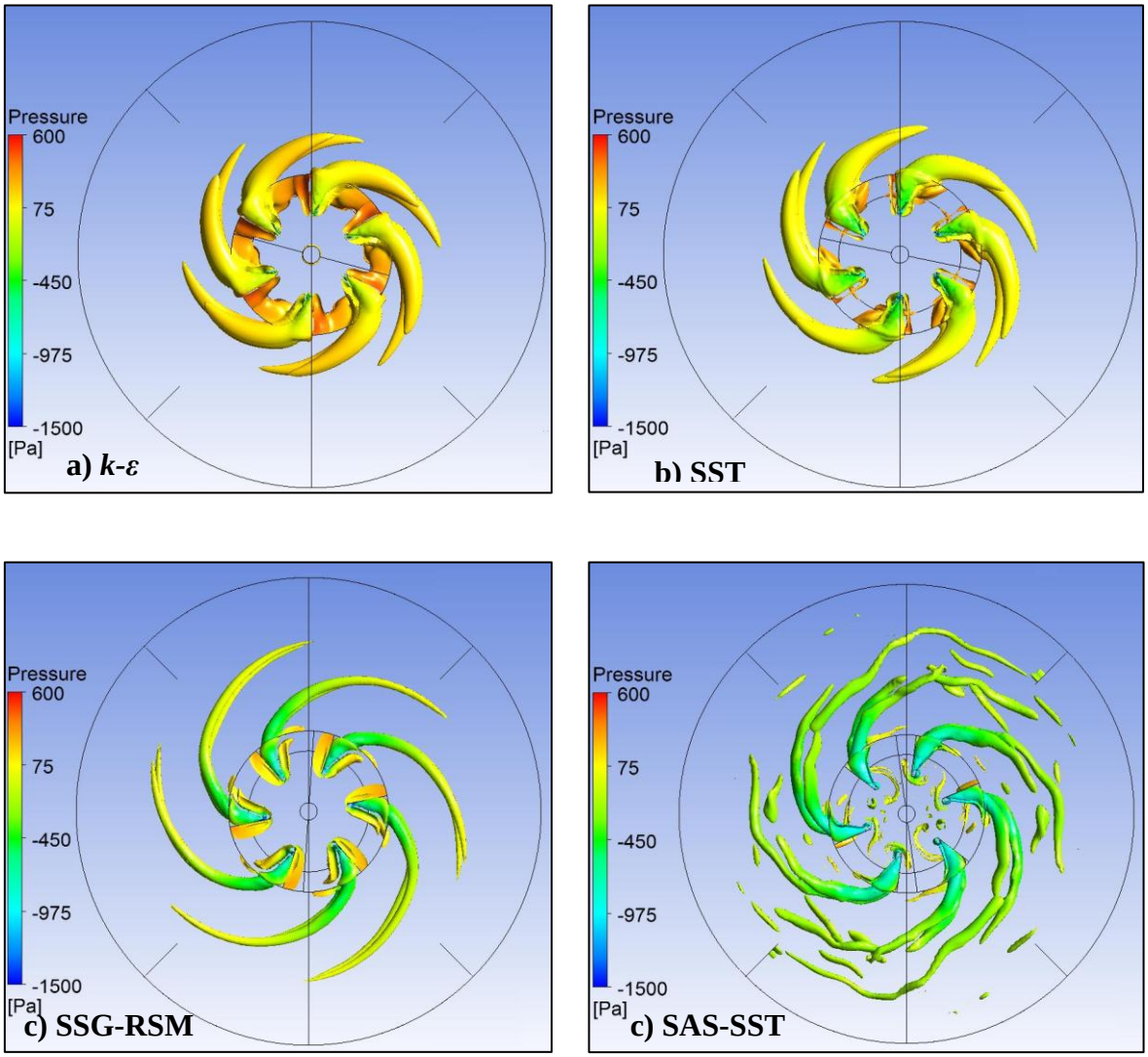

Figure 2-8: Trailing vortices visualized using a swirling strength of 0.1 for the *k*-*ε*, SST, SSG-RSM and SAS-SST turbulence models.

Unsteady two-equation models, such as *k*-*ε* and SST, are well-known for excessively damping turbulence so that any detail of the turbulent structure (even on the larger scales) cannot be resolved directly. This is reflected in Figures 2-8a and 2-8b, which show that these models predict very small and hence dissipative trailing vortices with no secondary vortex motion apparent. Nevertheless, both the *k*-*ε* and SST models predict the appearance of the pair of vortices, one vortex above and one vortex below the disk of the impeller, that originate from behind each blade and trail out into the bulk of the flow. Note that Honkanen *et al.* (2007) also predicted smooth, overly-dissipative trailing vortices with hardly any secondary motion using the SST turbulence model. In the *k*-*ε* and SST models, all turbulence scales are modelled through Reynolds-averaging, and hence a relatively

large length-scale of turbulence was calculated using Equations (2-16) and (2-17), as can be seen in Figures 2-9a and 2-9b. Curvature correction in the SST model had a minor effect on the length of the trailing vortices and the length-scales of turbulence - this comparison is not shown here - and therefore, from this perspective, it did not improve the SST predictions appreciably. Interestingly, the length-scales of turbulence of up to 3 mm predicted by the *k-ε* and SST models in the region of the impeller (shown in Figure 2-9) are similar to the experimental turbulence length-scales of between 0.3 and 3.0 mm measured by various researchers and compiled together by Wu and Patterson (1989).

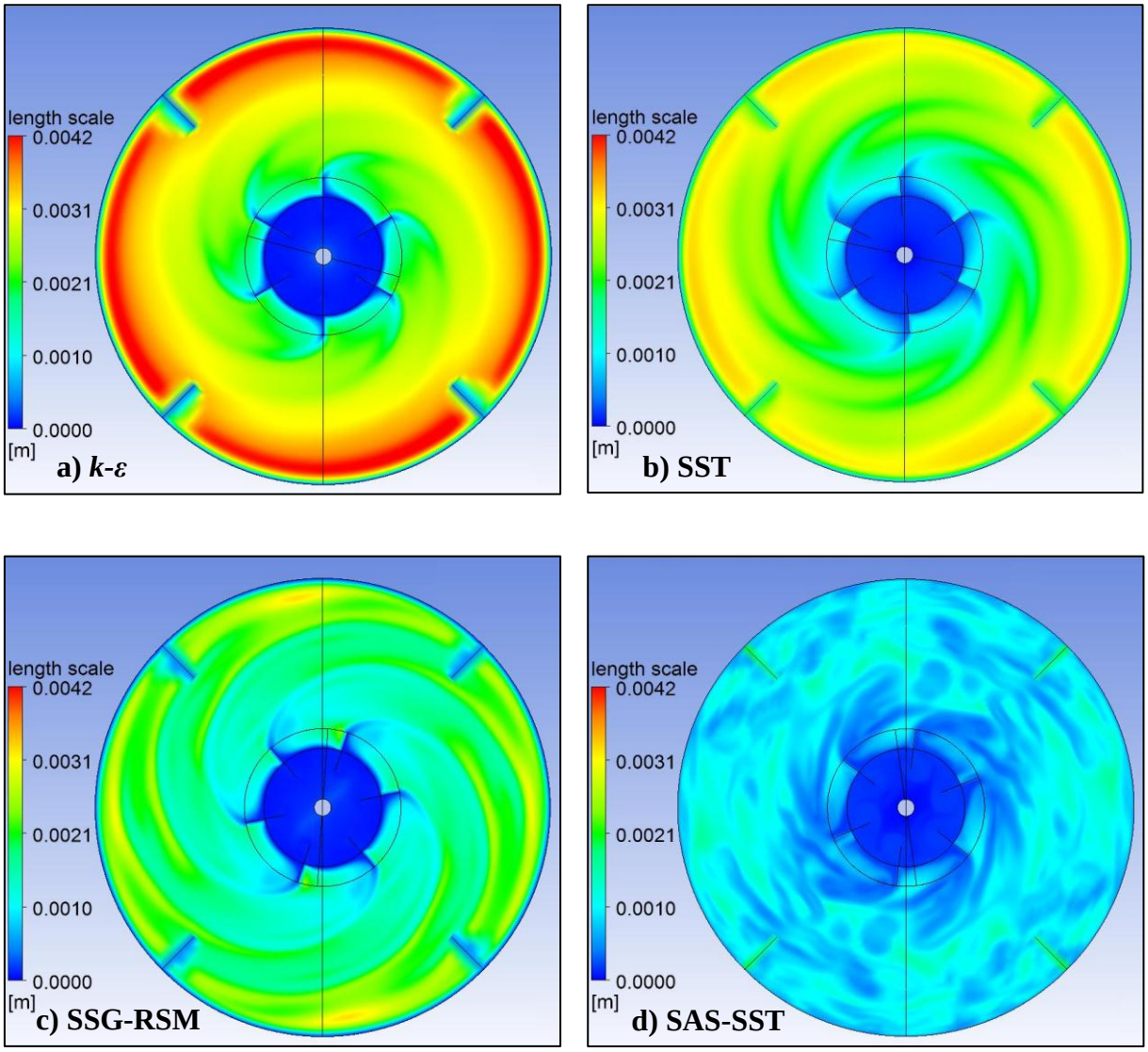

Figure 2-9: Predicted turbulence length scales for *k-ε*, SST, SSG-RSM and SAS-SST turbulence model simulations at the impeller disk elevation.

For the SAS-SST model, some details of the turbulence structures -the larger scale structures- can be directly resolved, while Reynolds averaging accounts for the smaller-scale turbulence structures. Figure 2-8d shows that the SAS-SST model predicts longer trailing vortices and secondary vortex motions, in agreement with Honkanen *et al.* (2007), who found that the SAS-SST model is able to predict vortices of comparable length and intensity to those found experimentally. The turbulence length-scales predicted by the SAS-SST model (Figure 2-9d) are much shorter than those predicted by the *k-ε* and SST models, because the larger scale turbulence is now being directly resolved through the "LES" content of the model. Figures 2-8c and 2-9c show that the SSG-RSM model is able to predict trailing vortices more similar to those predicted by the SAS-SST model, although no secondary motions are evident.

2.2.5 Power Number

Table 2-2 summarizes the predictions of the power number for the different turbulence models, calculated by the two different methods described in Section 2.1.5. By comparing these values with the power number of 5, which was assumed (not measured directly) by Wu and Patterson (1989) on the basis of measurements conducted by Bates *et al.* (1963), it can be seen that the power number determined from the torque on the impeller over predicts the experimental data by 14% for the *k-ε* model and at least 30% for the SST, SST-CC, SAS-SST and SSG-RSM models. Delafosse *et al.* (2008) found an over-prediction of the power number determined from the torque of 20% for the *k-ε* model. The predicted power number determined by integrating the turbulence energy dissipation rate throughout the fluid volume is close to the power number of 5 for nearly every turbulence model tested.

There is, however, a question of whether an assumed power number of 5 is reasonable, given that there were no data provided on the thickness of the impeller blades in the paper of Wu and Patterson (1989). In fact, the predicted power numbers determined from the torque in this paper are closer to the value of 6 measured by Rushton *et al.* (1950). As described above, both Rutherford *et al.* (1996) and Delafosse *et al.* (2008) have shown that the power number increases with decreasing blade thickness. In the simulations presented here, an impeller with blades of negligible thickness was modelled and thus predicted power numbers at the higher end of the spectrum can be expected. Furthermore, Figure 2-

7 clearly shows an under-estimation of ε throughout the tank by all the turbulence models tested, and it is therefore reasonable to assume that the simulated power numbers based on the volume integral of ε are also under-predicted. Therefore, it is assumed in this paper that the predicted power number based on torque is more indicative of the actual power number than the predicted power number based on turbulence energy dissipation rate. It became clear during this work that CFD simulations of a stirred tank using a mesh that properly resolves the blade thickness would be impractical with the computing power available.

The width of the axial profile of turbulence energy dissipation rate at 1.07 r_R predicted by the SST-CC model is narrower than that of nearly every other turbulence model tested, as shown in Figure 2-7c. This lower turbulence energy dissipation rate in the vicinity of the impeller explains the relatively low power number (based on the volume integral of ε) of 4.5 predicted by the SST-CC model compared with the other turbulence models tested, as shown in Table 2-2. The predicted power number based on the volume integral of ε for the SSG-RSM model is highest at 5.5, because the predicted turbulence energy dissipation rate for this turbulence model becomes higher than for the other models radially away from the impeller tip, as shown in Figure 2-6. Note that the power number fluctuates as the impeller rotates, and the predicted range of these fluctuations is presented in Table 2-2.

Table 2-2: The effect of the turbulence model on power number calculated using the torque and volume-integral of the turbulence energy dissipation rate methods.

Turbulence model	Power number from torque	Power number from ε
k-ε	5.7± 0.2	5.1 ± 0.1
SST	6.5 ± 0.2	5.1 ± 0.04
SAS-SST	6.9 ± 0.7	5.2 ± 0.4
SSG-RSM	6.5 ± 0.3	5.5 ± 0.2
SST-CC	6.6 ± 0.3	4.5 ± 0.05

2.2.6 Computational Cost

Approximately five impeller revolutions were required to obtain a pseudo-steady state simulation for the *k-ε*, SST, SSG-RSM and SST-CC models. Only one further revolution was required for averaging purposes after the pseudo-steady state had been reached for these models. For the SAS-SST model, a large number of revolutions were required to

obtain good statistical averages. Thirty revolutions worth of data were collected in this study. Given that at least 20 revolutions were required for the SAS-SST model to obtain good statistical averages, the computational time required to obtain meaningful results from the SAS-SST model was at least twenty times greater than that required for the k-ε or the SST models. LES models are computationally even more intensive since they are more sensitive to the grid and therefore would require even more grid refinement (Menter & Egorov, 2005) and more impeller revolutions for good statistical averages. In an industrial setting, the solution time is likely to be an important factor affecting the choice of turbulence models in the simulation of turbulent flow in stirred tanks. From this point of view, the SST model with curvature correction is the most attractive choice, since it provides a reasonably accurate solution in the lowest computational time.

2.3 Nomenclature

C_μ	A constant in the definition of the turbulence length scale
D	Diameter of tank
k	Modelled turbulence kinetic energy
k_p	Periodic kinetic energy
k_{p+le-r}	Periodic kinetic energy plus the turbulence (random) kinetic energy due to large-eddies in SAS-SST model
k_r	Turbulence (random) kinetic energy
k_t	Total kinetic energy of fluctuating motions
l	Turbulence length-scale
N	Number of time-steps
N	Rotational speed
$N_{P\tau}$	Power number measured through torque on the impeller
$N_{P\varepsilon}$	Power measured by integrating turbulence energy dissipation rate over the tank volume
n_{TS}	Number of full turns of the impeller
R	Radial distance from the center of rotation
R	Impeller radius
r_R	r/R
u'	Velocity fluctuations in the radial direction
$\bar{u}$	Mean velocity
u_i	Transient velocity
u_{ins}	Instantaneous velocity
u_{le-r}	Random velocity due to the large eddies
u_p	Periodic velocity
u_r	Random velocity

U_r	Radial velocity
$u_{se\text{-}r}$	Random velocity due to the smaller eddies
U_{tip}	Impeller tip velocity
U_z	Axial velocity
U_θ	Tangential velocity
v'	Velocity fluctuations in the tangential direction
W	Width of the blade
w'	Velocity fluctuations in the axial direction
Z	Axial distance from the center of impeller
z_w	2z/W

Greek Letters

E	Turbulence energy dissipation rate
ε_{avg}	Average turbulence energy dissipation rate
P	Density
T	Torque
Ω	Turbulence eddy frequency

3 Oxygen transfer rate experiments

The availability of sufficient oxygen is of utmost importance when culturing cells or micro-organisms in a bio-reactor. Oxygen can be supplied by bubbling air through the culture medium or by passing air through a gas-permeable membrane contained within the tank. Appropriate air flow rates and agitation speeds must be chosen, since they affect the rate of oxygen transfer to the micro-organisms. A good understanding of the oxygen transfer rate and the oxygen demand of cells will help in establishing optimal operating conditions for culturing cells in stirred tanks. One of the main objectives of this particular study is to find similar oxygen transfer rates for oxygenation via air bubbling and a gas-permeable membrane with the same agitation speeds.

Although bubbling air is the most commonly used and the most efficient method for oxygenation, it can damage cells, especially animal cells, which have no cell wall and are therefore sensitive to the fluid mechanical stress associated with the rising and bursting of bubbles (Tramper, *et al.*, 1986). Alternative oxygenation methods that result in low fluid mechanical stresses have been sought in the past. Smith and Greenfield (1992) used headspace gassing with air or oxygen in a stirred tank. However, headspace gassing is limited to smaller sized vessels of order 500 ml due to the limitations of low interfacial area (surface area of the gas phase to the volume of liquid phase) inside larger vessels, which renders oxygen transfer inefficient (Singh, 1999). Porous membranes of silicon (Kunas & Papoutsakis, 1990) or Polytetraflouroethylene / Teflon (PTFE) (Schneider, *et al.*, 1995) have also been used for oxygenation. The advantage of using porous membranes is that higher agitation speeds are possible by avoiding cell damage caused by bubbling.

Kunas and Papoutsakis (1990) proposed that aeration via bubbling and/or agitation are the two fluid mechanical forces mostly responsible for cell damage. However, it is not known which of these mechanical forces is more influential on the cells. The impact of each of these forces on the cells should be quantified not only for better understanding of this phenomenon but also for better optimization of the process. There has been no research so far that has separated the cell damage due to these two hydrodynamic forces. One possible experiment to separate these forces involves oxygenating cells in a stirred tank first using standard air bubbling and then using a gas-permeable membrane. By comparing the cell

damage resulting from each type of oxygenation method for a given agitation rate, the effect of bubbling versus no bubbling can be ascertained. The study of Schneider *et al.* (1995) has laid the foundation for this study by reporting on experiments where PTFE tubing was used to oxygenate the culture medium.

In this chapter, operating conditions that result in appropriate oxygenation rates for cell culturing are chosen for both air-bubbling and gas-permeable membrane oxygenation. In this preliminary experiment, no cells will be cultured, only oxygen transfer rates will be measured. The procedure is 1) to conduct experiments at various agitation speeds and air flow rates for both bubbling and gas-permeable membrane; 2) to calculate the oxygen transfer rate for both cases; 3) to compare the oxygen transfer rates of both of these cases and choose a similar value for a given agitation speed that results in appropriate oxygenation during cell culturing, as determined from the literature. This information can be used in future experiments in which cells are cultured using either air-bubbling or a gas-permeable membrane for oxygenation. The extent of cell damage due to bubbling could then be ascertained by comparison. It is important to note that the air flow rate and percentage of oxygen in the air will be varied in order to keep similar oxygen transfer rates.

3.1 Mass transfer theory

3.1.1 Bubbling experiments

For a bubble present in a liquid phase, the amount of mass transferred from its surface into the liquid is proportional to the concentration difference and the interfacial area (Mills, 1999). The major resistance is observed in the liquid film surrounding the gas bubble (Figure 3-1). Hence, the transport of oxygen through the liquid film can be expressed as:

$$N_A = k_L(C_{Asat} - C_A) \tag{3-1}$$

where N_A is the flux at the interface, k_L is the mass transfer coefficient in the liquid phase, C_{Asat} is the saturated concentration at the surface of the bubble and C_A is the bulk concentration of the dissolved oxygen.

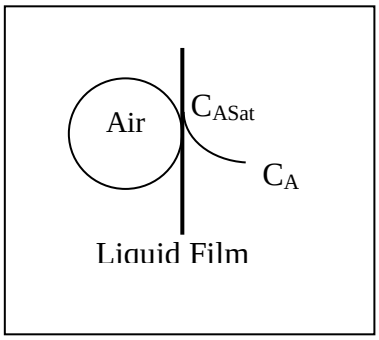

Figure 3-1: Oxygen concentration profile at air bubble-medium interface

In a closed reactor, the oxygen consumption can be expressed as:

$$\frac{d}{dt}VC_A = AN_A = Ak_L(C_{Asat} - C_A) \tag{3-2}$$

which can be rearranged as follows

$$\frac{dC_A}{(C_{Asat} - C_A)} = \frac{Ak_L}{V}dt \tag{3-3}$$

and integrated to give

$$-ln(C_{Asat} - C_A) = k_L a_b t + B \tag{3-4}$$

Here a_b is the ratio of area of oxygen bubbles to the volume of the liquid phase and B is a constant of integration. At initial conditions when t=0, it can be supposed that $C_A = C_{A0}$, which implies that $B = -ln(C_{Asat} - C_{A0})$. Therefore, Equation 4 becomes:

$$k_L a_b = ln\frac{(C_{Asat}-C_{A0})}{(C_{Asat}-C_A)}/t \tag{3-5}$$

3.1.2 Membrane experiments

In the case of the transfer of oxygen through the gas-permeable membrane, the gas phase is present within the gas-permeable membrane tube, with the membrane wall acting as a resistance to the transfer of oxygen to the liquid phase (Schneider, *et al*., 1995). Two other resistances include the gas film (on the inner-tube side) and the liquid film (on the outer-tube side), as shown in Figure 3-2. It can be assumed that there is an overall mass transfer coefficient, k_m which has contributions from the mass transfer coefficients due to the gas film, k_G, the thickness of the gas-permeable membrane, k_t, and the liquid film, k_L. Hence, the transfer of oxygen can be expressed as:

$$N_A = k_m(C_1 - C_2) \tag{3-6}$$

where C_1 is the concentration of oxygen inside the gas-permeable membrane tube and C_2 is the concentration in the bulk liquid. C_2 was measured directly by the dissolved oxygen probe in percentages. Appendix 7.2 shows the details of the determination of C_1, which should be the concentration of oxygen in the air within the gas permeable membrane tube if k_m is the overall resistance across the membrane. In Appendix 7.2, it is reasoned from experiment that C_1 is equal to the saturation concentration of oxygen in water. Again, the oxygen consumption can be expressed as:

$$\frac{d}{dt}VC_2 = AN_A = Ak_m(C_1 - C_2) \tag{3-7}$$

Following the same procedure as followed in Equation 3-5, $k_m a_m$ can be obtained as:

$$k_m a_m = ln\frac{(C_1-C_0)}{(C_1-C_2)}/t \tag{3-8}$$

where a_m represents the ratio of surface are of gas-permeable membrane to the volume of the liquid phase.

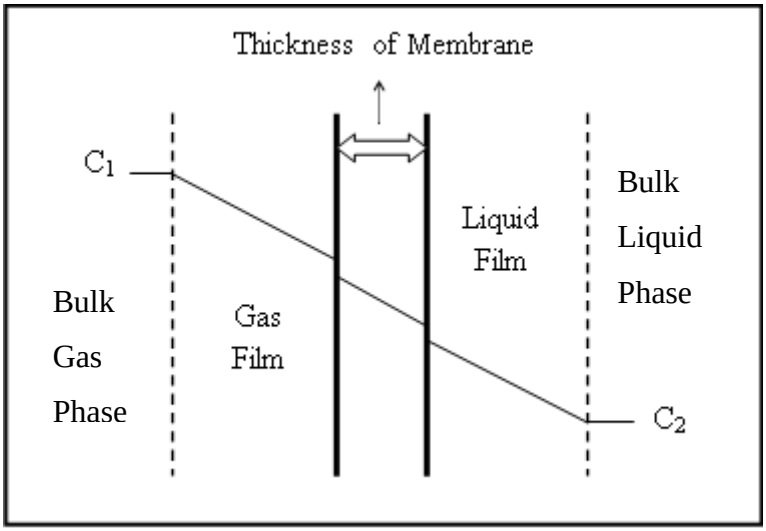

Figure 3-2: Transfer of oxygen through a gas-permeable membrane into the Bulk Liquid Phase

3.2 Materials and methods

3.2.1 Membrane for bubble-free oxygenation

In order to achieve bubble-free oxygenation, a suitable membrane is required to provide the oxygen in the liquid phase (Figure 3-3). This can be done either by providing air/oxygen in liquid phase or in gas phase within the gas-permeable membrane tube, from where the oxygen diffuses through the pores of the membrane and mixes with the surrounding liquid phase without producing any bubbles. Schneider *et al.* (1995) have shown that the overall mass transfer coefficient is much less when the air/oxygen is in the liquid phase within the permeable membrane tube compared with air/oxygen in the gas phase. Therefore, only gas-phase oxygenation was considered in this work.

Typically, there are three types of gas permeable membranes that can be used for membrane-based gas absorption processes: 1) nonporous or dense film membranes such as silicone rubber membranes; 2) microporous membranes made of glassy polymers, such as polypropylene or polyethersulfone and; 3) composite material made of polydimethylsiloxane (PDMS) / polypropylene (PP) and polyalkylsulphone (PAS) / PP (Vladisavljevic, 1999; Voss, Ahmed, & Semmens, 1999). Each membrane type has certain advantages and disadvantages. Nonporous/dense film membranes such as silicon rubber membranes can be operated at high trans-membrane pressures without forming

bubbles. Silicon-rubber membranes also have high gas permeability (Table 3-1). However, there is a problem of bio film attachment and growth. This problem can be resolved by providing pure oxygen within the membrane tube because with pure oxygen, the oxygen concentration at the solid-liquid interface increases to a toxic level for any bio film (Wilderer, Bräutigam, & Sekoulov, 1985). However, this solution involves the additional cost of providing a continuous supply of pure oxygen.

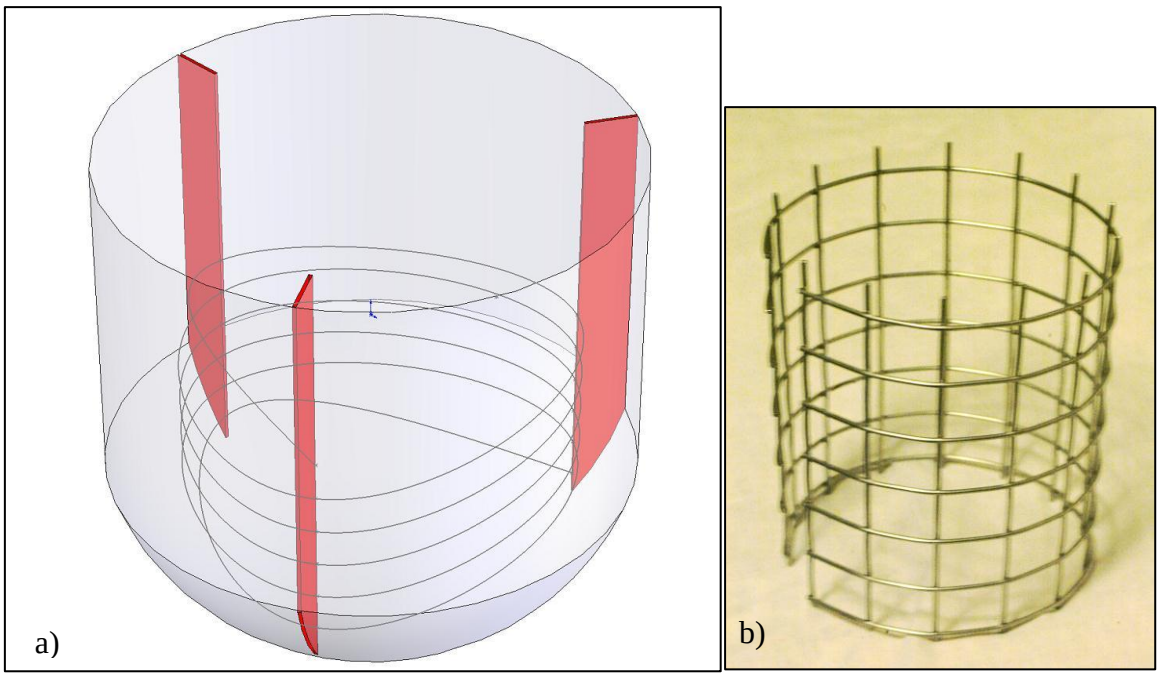

Figure 3-3: Installation of gas-permeable membrane (a) in a spiral shape around the inside of a mesh (b) in the stirred tank.

The advantage of using microporous membranes is their better gas permeabilities and the possibility of manufacturing as small diameter hollow fibers (100–400 µm) to provide a very high interfacial area per unit volume (Vladisavljevic, 1999). However, microporous membranes cannot be operated at higher operating pressures due to the formation of bubbles above 14 kPa (2 psi) (Voss, *et al.*, 1999). Voss *et al.* (1999) found that when microporous hollow fibers are coated with an ultrathin (approximately 1 µm) nonporous layer of composite material, such as PDMS, the membrane can be operated at oxygen pressures as high as 410 kPa (60 psi) without bubble formation in water which is maintained at atmospheric pressure. Ahmed *et al.* (2004) found that the polyurethane layer and the fiber arrangement allowed the usage of high operating pressures. Such an

arrangement enhanced the rate of oxygen transfer drastically, irrespective of the presence of membrane resistance, and resulted in 100% oxygen transfer efficiency. Therefore, Ahmed *et al.* (2004) observed better oxygen transfer rates using composite fiber membranes compared with polypropylene fiber membranes. The biggest disadvantage of these membranes was the high cost and availability of a vendor.

However, the PTFE membrane, which is another type of microporous membrane, shows great promise as well. Schneider *et al.* (1995) found that the PTFE membranes give twice the oxygen transfer per unit surface area of membrane compared with silicon tubing. PTFE membranes have high gas permeability (Table 3-1) and are hydrophobic in nature; thus they completely prevent cell growth on the membrane surface. Most importantly, these membranes have been successfully used to culture insect cells at various agitation speeds eliminating the need to oxygenate via bubbles. Finally, these membranes are relatively inexpensive and readily available. Considering these advantages, it was decided to work with the PTFE membranes in this work.

Table 3-1: Oxygen permeability through various organic materials. Data from Lynch W. (1978) provided by Wilderer *et al.* (1985)

Material	Permeability (cm^3, mm/cm, cm Hg, sec) x 10^{-10}
Polyamide	0.38
Polyvinyl chloride	1.2-6
Hexafluor Propylene	15
Polyethylene	11-59
Ethyl cellulose	265
Natural rubber	230
Silicone rubber	5,000-6,000
PTFE (Heller, Pasternak, & Christensen, 1970)	420 cB = (cm^2 - cm) / (cm - Hg - sec - cm^2) x 10^{-8}

3.2.2 Equipment used

A stirred tank was used as the reactor for the experiments. The advantages of using a stirred tank are many. Firstly, a vast amount of experimental data for stirred tanks exists in the literature which can be used for validation purposes. Secondly, using a stirred tank provides an opportunity to separate the two major causes of cell damage in a bio-reactor, namely, damage caused by bubbles and damage caused by agitation. This is possible if oxygen can be provided to the animal cells by using membranes so that there is no bubble-generation in the reactor (Schneider, *et al.*, 1995). In other reactors, such as the bubble column and air-lift reactors, bubbles are required to produce recirculation and so the shear stress effects generated by bubbles and velocity gradients would be difficult to separate. Spinner flasks were also considered for investigation in this project. However, the maximum agitation that can be achieved in these reactors is very low, so that shear generation would be negligible. Finally, stirred tanks can be modelled easily with CFD to obtain the flow profiles of velocity, turbulence kinetic energy, and most importantly turbulence energy dissipation rate (Delafosse, *et al.*, 2008), which has been correlated closely to cell damage by various researchers (Ma, Koelling, & Chalmers, 2002; Mollet, *et al.*, 2007; Mollet, Godoy-Silva, Berdugo, & Chalmers, 2008).

Figure 3-4 shows an overview of the complete equipment used in this study. The stirred tank as shown in Figure 4-1 is cylindrical in shape and contains a standard six-blade Rushton turbine and three equally spaced baffles that are attached to the tank wall. A J-shaped pipe was used to produce bubbles which appeared a few centimetres underneath the six-blade Rushton turbine. The gas-permeable membrane was installed in a spiral shape (Figure 3-3a) around the inside of a circular mesh (Figure 3-3b), whose outer-diameter was equal to the inner diameter of the baffles. The gas-permeable membrane had an external diameter of 6 mm and length of 2.2 m. Dissolved oxygen concentration was measured on-line using a dissolved oxygen meter. A specific probe for controlling temperature was also used. This cylindrical stirred tank also has options for controlling pH, on-line cell density measurement, managing feed pumps automatically for culturing cells, controlling foam with automatic antifoam unit, analysing output gas, and taking samples.

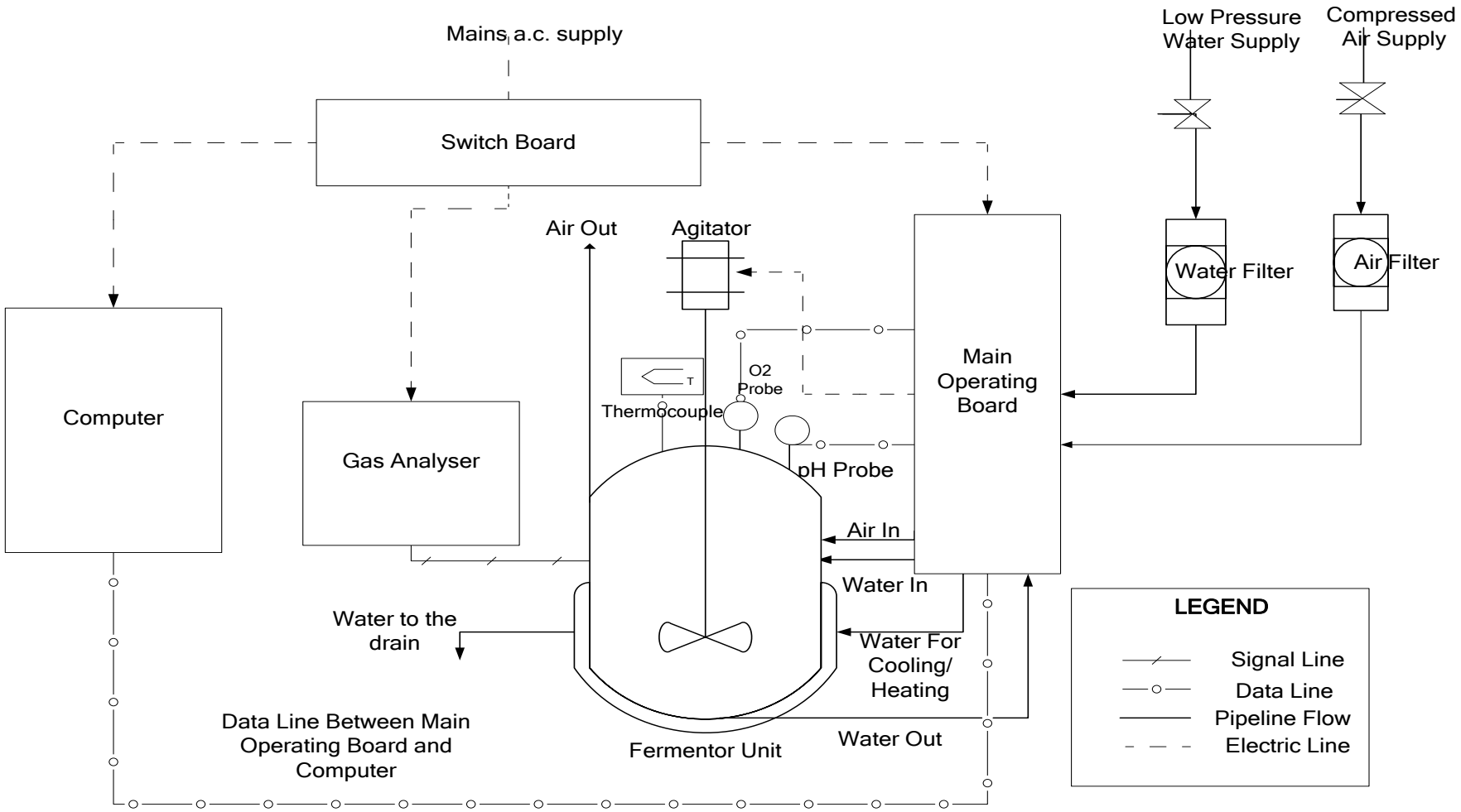

Figure 3-4: Stirred tank used for oxygenation by bubbling and through a gas-permeable membrane.

3.3 Results and discussion

Repeated measurements of oxygen transfer rate for a few selected values of gas flow rates and rotational speeds were carried out at-least 4 times for k_La_b, and k_ma_m measurements. The relative deviation from the average value was ≤ 2.5 % for bubbling experiments and 2.1 % for gas-permeable membrane experiments.

3.3.1 Calculating oxygen transfer rate

Oxygen transfer rates were calculated using Equations 3-5 and 3-8, respectively, for the bubbling and gas-permeable membrane experiments. Figure 3-5 shows that, apart from the initial phase of oxygen transfer rate for bubbling experiments which seems to be exponential in nature, the overall oxygen transfer rate follows a linear pattern. The deviation from linearity is comparatively higher with the increase in the gas flow rate. In contrast, in the case of membrane experiments, the oxygen transfer rate completely follows the linear first order equation.

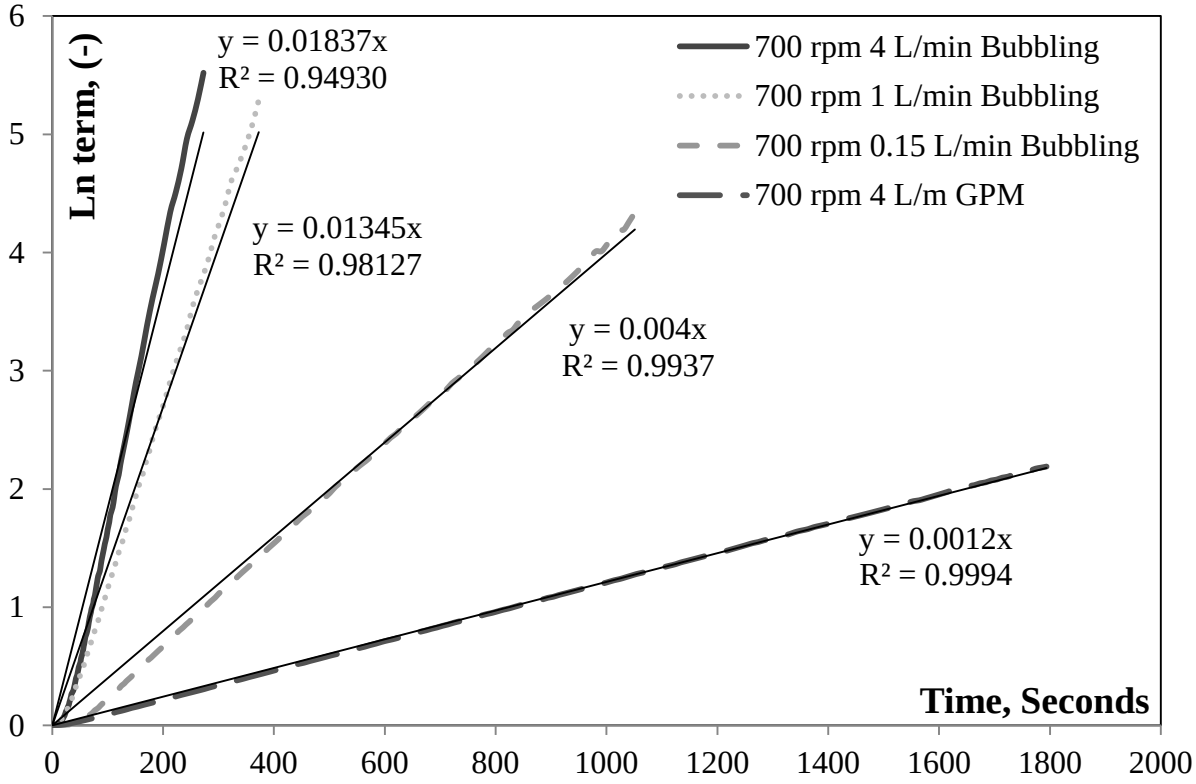

Figure 3-5: Oxygen transfer rate at different gas flow rates when oxygenation is carried out by bubbling and through gas-permeable membrane (GPM) at a constant rotational speed of 700 rpm and at an oxygen concentration of 21% in the air.

3.3.2 Comparison of oxygen transfer rate with gas flow rate

In Figure 3-6, it can be observed that there is an increase in the oxygen transfer rate with k_La_b increasing from 0.00399 to 0.01837 when the gas flow rate is increased from 0.15 to 4 L/min. Table 3-2, however, indicates that when the gas-permeable membrane was used the gas flow rate had little effect on the oxygen transfer rates. This minor effect of gas flow rates is due to low gas-side resistance to the oxygen transfer compared with the resistance within the membrane wall and the liquid side resistance. In the case of bubbling, the increase in the gas flow rate increases the number of bubbles produced by the sparger and hence the surface area, thus leading to an increase in the oxygen transfer rate.

Table 3-2: Oxygen transfer rates for gas-permeable membrane at different gas flow rates and oxygen concentrations in the air for a constant rotational speed of 700 rpm.

700 rpm		
Gas flow rate, L/m	Oxygen transfer rate, k_ma_m, s^{-1}	Oxygen concentration in the air, %
2	0.00138	21
3	0.00134	21
4	0.00146	21
4	0.00140	30
4	0.00146	40

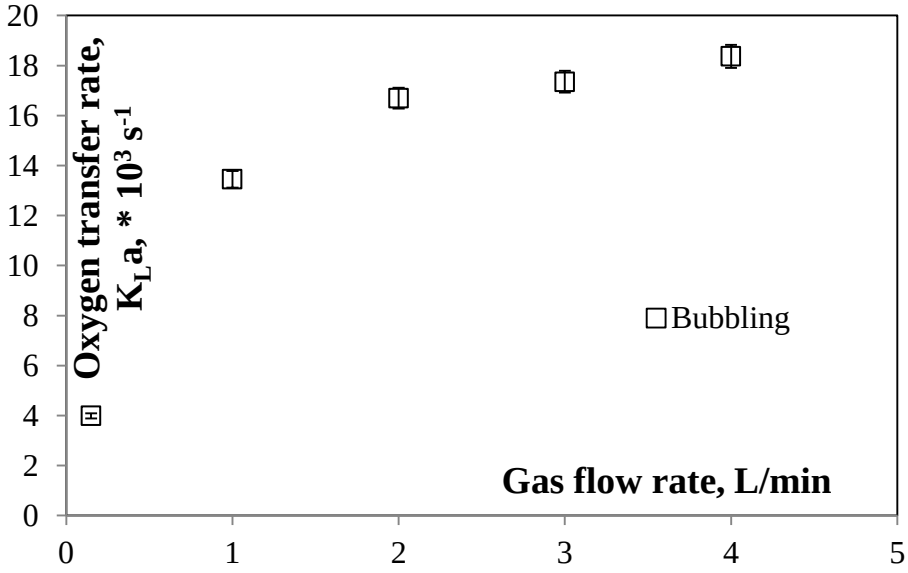

Figure 3-6: Comparison of oxygen transfer rate with the gas flow rate at a constant rotational speed of 700 rpm.

Another important point to observe is that even the increase in the oxygen concentration in the gas flow rate does not impact significantly the oxygen transfer rate when oxygenation is carried out using a gas-permeable membrane (Table 3-2). Schnieder *et al.* (1995) found relatively lower oxygen transfer coefficients when they used pure oxygen compared with air while using a similar PTFE gas-permeable membrane. In contrast, Wilderer *et al.* (1985) reported higher oxygen transfer rates when they used pure oxygen in comparison with air with a silicon based gas-permeable membrane. In their cell culturing experiments, they found growth and development of biofilm around the gas-permeable membrane when they used air; whereas, this growth and development of biofilm was inhibited when they used pure oxygen, which they attributed to the probability of toxic levels of oxygen for the cells at the membrane-liquid interface.

3.3.3 Comparison of oxygen transfer rate with rotational speeds

Figure 3-7 shows a linear increase in the overall oxygen transfer rate for gas-permeable membrane, $k_m a_m$, and for bubbling, $k_L a_b$, with increase in the rotational speed. In this figure, the mass transfer coefficients for the lowest tested gas flow rate for bubbling are compared with the mass transfer coefficients for the highest tested gas flow rate for gas-permeable membranes. Even with a very low gas flow rate in the bubbling experiment, the oxygen transfer rate when bubbling is always considerably higher than the oxygen transfer rate for the gas-permeable membrane. This is true even when high oxygen concentrations (up to 40% tested in this work) are used in the gas-permeable membrane. Under similar conditions of gas flow rate and rotational speed, the oxygen transfer rate is at-least 10 times higher for bubbling experiments in comparison with the gas-permeable membranes.

These experiments were carried out to observe if there would be sufficient oxygen when culturing cells in the stirred tank for a given set of operating conditions. The maximum overall oxygen transfer coefficient, $k_{m,}$ measured by Schneider *et al.* (1995), who successfully cultured insect cells using PTFE gas-permeable membrane in a stirred tank similar to the one used in this study, was approximately 1.6×10^{-5} m/s at a rotational speed of 250 rpm and air flow rate of 1.4 L/min. In the experiments reported here, at an air flow rate of 4 L/min and a comparable rotational speed of 300 rpm, the overall oxygen transfer coefficient was found to be approximately 4.0×10^{-5} m/s. This increase in the overall oxygen transfer coefficient is due to the 2.2 metre length of gas-permeable membrane used

in the experiments reported here compared with 0.6 m used by Schneider *et al.* (1995). The research work of Singh (1999) shows that an overall oxygen transfer rate of greater than 1 hr^{-1} is sufficient for cell culture. In this work, the minimum oxygen transfer rate with the gas-permeable membranes was always greater than 2 hr^{-1}. Hence, the gas-permeable membrane investigated here can be used to provide sufficient oxygenation for culturing animal cells in the stirred tank of this work.

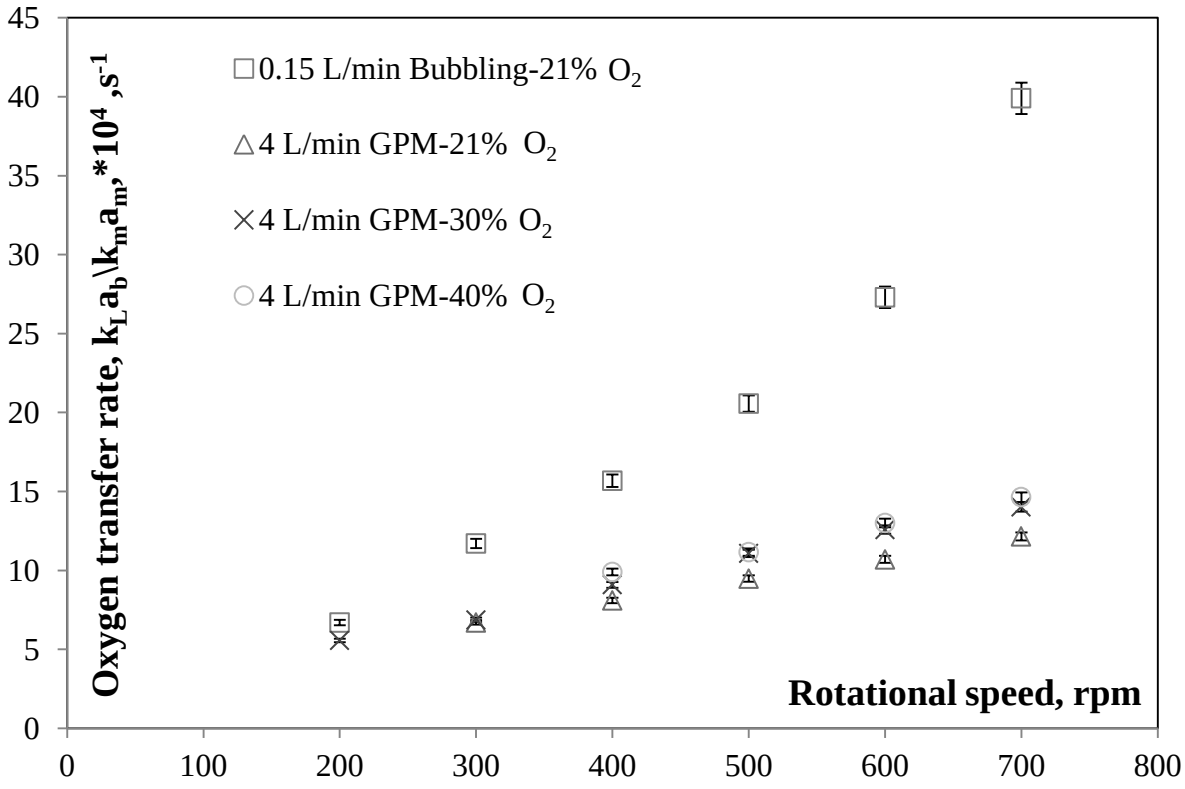

Figure 3-7: Comparison of the overall oxygen transfer rates for gas-permeable membrane (GPM), $k_m a_m$, and bubbling, $k_L a_b$, experiments at different rotational speeds and oxygen concentrations.

3.4 Nomenclature

a_b	Interfacial area = A/V for bubbling
a_m	Interfacial area = A/V for gas-permeable membrane
A	Area of the gaseous phase
B	Constant of integration
C_0	Initial concentration of the dissolved oxygen at time t =0 when gas-permeable membrane is used for oxygenation
C_1	Concentration of oxygen inside the gas-permeable membrane
C_2	Bulk concentration of the dissolved oxygen when gas-permeable membrane is used for oxygenation
C_A	Bulk concentration of the dissolved oxygen when bubbling is used for oxygenation
C_{A0}	Initial concentration of the dissolved oxygen at time t =0 when bubbling is used for oxygenation
C_{Asat}	Saturated concentration at the surface of the bubble
k_G	Mass transfer coefficient due to gas film
k_L	Mass transfer coefficient due to liquid film
k_m	Overall mass transfer coefficient for gas-permeable membrane
k_t	Mass transfer coefficient due to the thickness of the gas-permeable membrane
N_A	Flux at the interface
t	Time
V	Volume of the liquid phase

4 Operating Conditions based on parameters obtained through CFD

Over the years, researchers have shown experimentally the vulnerability of shear sensitive cells to the hydrodynamic forces that occur in a stirred tank reactor. Often, in these experiments, relationships for the shear sensitivity of the cells are found by correlating cell damage/death against a certain parameter, specific to the flow. However, the chosen parameter, such as impeller tip-speed or rotational speed, are usually vessel specific in these studies, and are thus not applicable for different vessel sizes and designs, as shown in Table 1-1. Therefore, a new vessel design requires new experiments in order to determine appropriate conditions for optimal culturing of cells, which is not only costly but also time consuming. There is an on-going search for a flow parameter that can be related to cell damage/death, which is general in nature and which can be obtained locally, (Garcia-Briones and Chalmers, (1994)). Turbulence energy dissipation rate is one such parameter which has taken the limelight in recent years. Gregoriades *et al.* (2000) showed an increase in the percent cell damage for microcarrier culture of Chinese hamster ovary (CHO) cells with an increase in maximum turbulence energy dissipation rate in a flow contraction device designed to capture the effects of shear and extensional flow on the cells. They used Computational Fluid Dynamics (CFD) to determine the turbulence energy dissipation rate in the flow contraction device. They found that the percent cell damage was below 10% up to a local maximum turbulence energy dissipation rate in the device of 10 m^2/s^3. Above this value, the percent cell damage increased significantly and reached around 80 % cell damage at a turbulence energy dissipation rate of 7×10^4 m^2/s^3. These results suggest that an upper limit on the turbulence energy disipation rate exists to avoid cell damage in a stirred-tank reactor. This would be controlled using the impeller rotational speed.

Continuing on from the work of Gregoriades *et al.* (2000), Ma *et al.* (2002) presented cell damage/rupture as a function of turbulence energy dissipation rate for 4 suspended cell lines, namely Chinese hamster ovary (CHO), spodoptera frugiperda (Sf-9), mouse hybridoma (HB-24), and human breast carcinoma (MCF7). They worked with a microfluidic channel - to capture the effects of shear and extensional flow on the cells, and conducted two-dimensional CFD simulations of the microfluidic device to estimate the turbulence energy dissipation rate. The percent cell damage was found to be below 10 %

for most of the cell lines up to a local maximum turbulence energy dissipation rate of 10^5 m^2/s^3. Above this, turbulence energy dissipation rate, the percent cell damage increased rapidly. The studies of Gregoriades *et al.* (2000) and Ma *et al.* (2002) show a relationship between turbulence energy dissipation rate, estimated via CFD, and cell damage/death measured experimentally. However, these workers studied simpler flow systems than usually employed in culturing cells, for which stirred tanks are often used, and their CFD studies do not give details of the turbulence model, grid independent study and the validation of the CFD model. In Chapter 2, the importance of validating the CFD model (linked to the choice of turbulence model and the grid and time-step independence study) has been demonstrated for the accurate estimation of the turbulence energy dissipation rate.

Table 4-1: Hydrodynamics used in the stirred tank reactors in different studies.

Ref.	Method of aeration	Rotational speed		Impeller tip speed	Reynolds number
		Rpm	Rps	m/s	(-)
Kunas and Papoutsakis (1990)	Gas-permeable membrane or headspace gassing	60 – 900	1.7 – 15	0.12 – 1.05	8,167 – 73,500
Smith and Greenfield (1992)	Headspace gassing	100 – 600	1.7 – 10.0	0.08 – 0.5	4,167 – 25,000
This study	Gas-permeable membrane	300 – 900	5.0 – 15.0	0.25 – 0.75	12,500 – 37,500

The main aim of this section is to model the stirred tank reactor used in the oxygenation experiments, detailed in Chapter 3, using the validated CFD model as a starting point. Results of Chapter 2 show that the SST model with curvature correction predicts the location and magnitude of maximum turbulence energy dissipation rate most accurately. Therefore, the SST-CC model will be used as the turbulence model to estimate the maximum turbulence energy dissipation rate at different rotational speeds. This study aims to create a sound base for future work to experimentally measure cell death rates for a range of impeller rotational speeds in the stirred tank reactor used in the oxygenation experiments, and to develop a correlation of the experimental cell death rates as a function of turbulence energy dissipation rate, determined using CFD. The ultimate aim is to produce a tool for predicting optimal operating conditions for culturing cells in stirred tank reactors of any scale.

4.1 The Computational Model

4.1.1 Description of the stirred tank

The stirred tank and Rushton turbine configurations used in the oxygenation experiments are shown in Figure 4-1. The tank has a diameter, D_t, and height, H, of 150 mm with three equally spaced baffles of width, J, one-tenth of the tank diameter. The diameter of impeller, D_a, is one-third of the tank diameter with 6 blades and is located at height, E, of one-third of the tank diameter from the base of the tank. The length, L, and width, W, of the blades are one-quarter and one-fifth of the impeller diameter, respectively. Water at 25 ^oC was used as the working fluid. Impeller rotational speed was modelled from 300-900 rpm, which corresponds to the Reynolds number from 12500 - 37500.

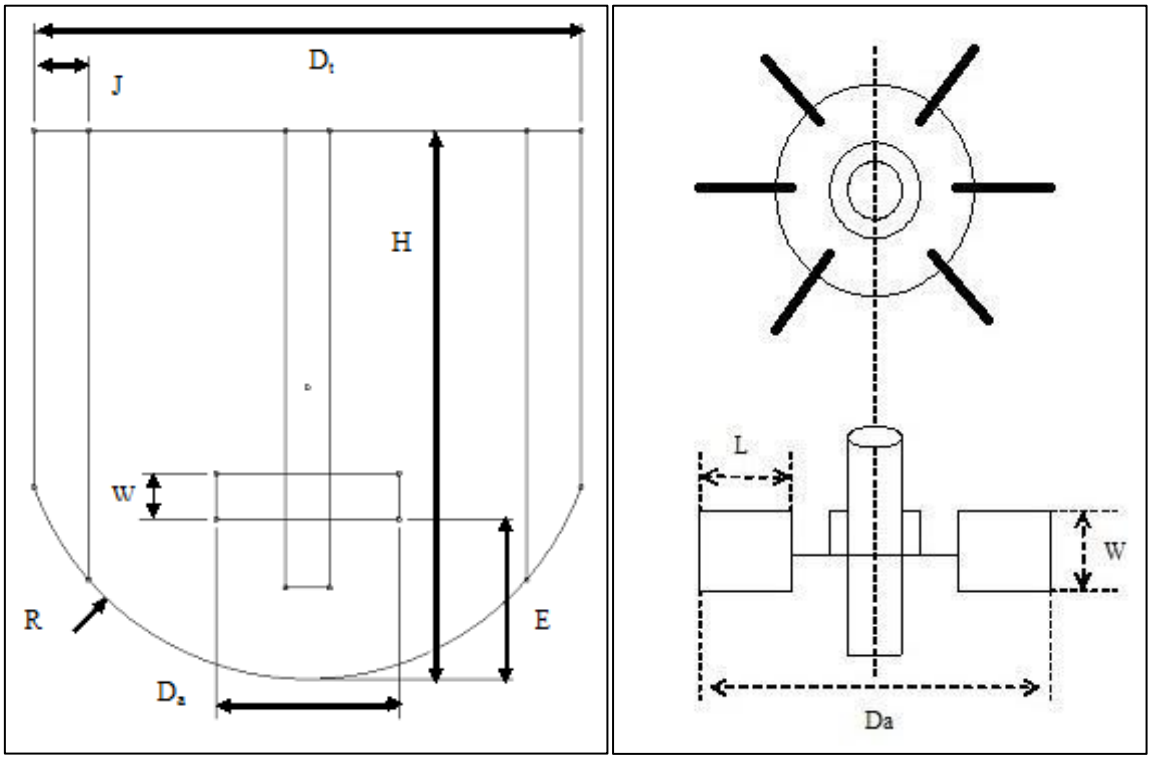

Figure 4-1: Configurations of the stirred tank and Rushton turbine.

4.1.2 Turbulence Modelling and Numerical scheme

Figure 2.6 shows that the SST-CC model estimates most accurately the magnitude and location of the maximum turbulence energy dissipation rate in a stirred tank. The SST-CC

model, developed by Smirnov and Menter (2009), is a modification to the SST model, that sensitizes it to streamline curvature and rotation.

All the simulations were carried out using the sliding mesh technique with the impeller swept region as the inner rotation zone and rest of the tank, including the baffles, as the stationary zone. No discontinuities in velocity, pressure, turbulence kinetic energy or turbulence energy dissipation rate were observed across the sliding interface with the mesh adopted in the simulations (Figure 4-2a and Figure 4-2b), which indicates a good resolution of the mesh across the interface (Figure 4-2c). The symmetry of the six-blade impeller and 3 baffles provided the opportunity to model only one-third of the geometry in order to reduce the computational effort. The thicknesses of the impeller blades, impeller disc and baffles were assumed to be zero to reduce the mesh complexity.

Based on the grid and time- step independence study done in the Chapter 2, a similar mesh of 1.472 million nodes and one degree resolution for the rotating impeller were chosen for the stirred tank. High resolution scheme was used for all equations for modelling the advection terms, and the transient terms were modelled using the second order backward Euler scheme. An RMS scaled residual of 10^{-5} was used as the convergence criteria for the continuity, momentum and turbulence quantities. A maximum of 10 iterations per time-step was set to achieve the convergence criteria for the SST-CC model. All simulations used double precision arithmetic. In these simulations, an un-converged steady-state simulation was used as the initial guess for the transient simulations. Collection of transient data was started only after a pseudo-steady state was achieved for all turbulence models.

Only one revolution of data was collected for the SST-CC model since repeat revolutions produced repeat data. The simulations have been performed using eight 1.9 GHz parallel processors each with 2 GB of memory. The simulation time of one revolution with one degree resolution in time-step and with a mesh having 1.472 million nodes was achieved in about 36 hours.

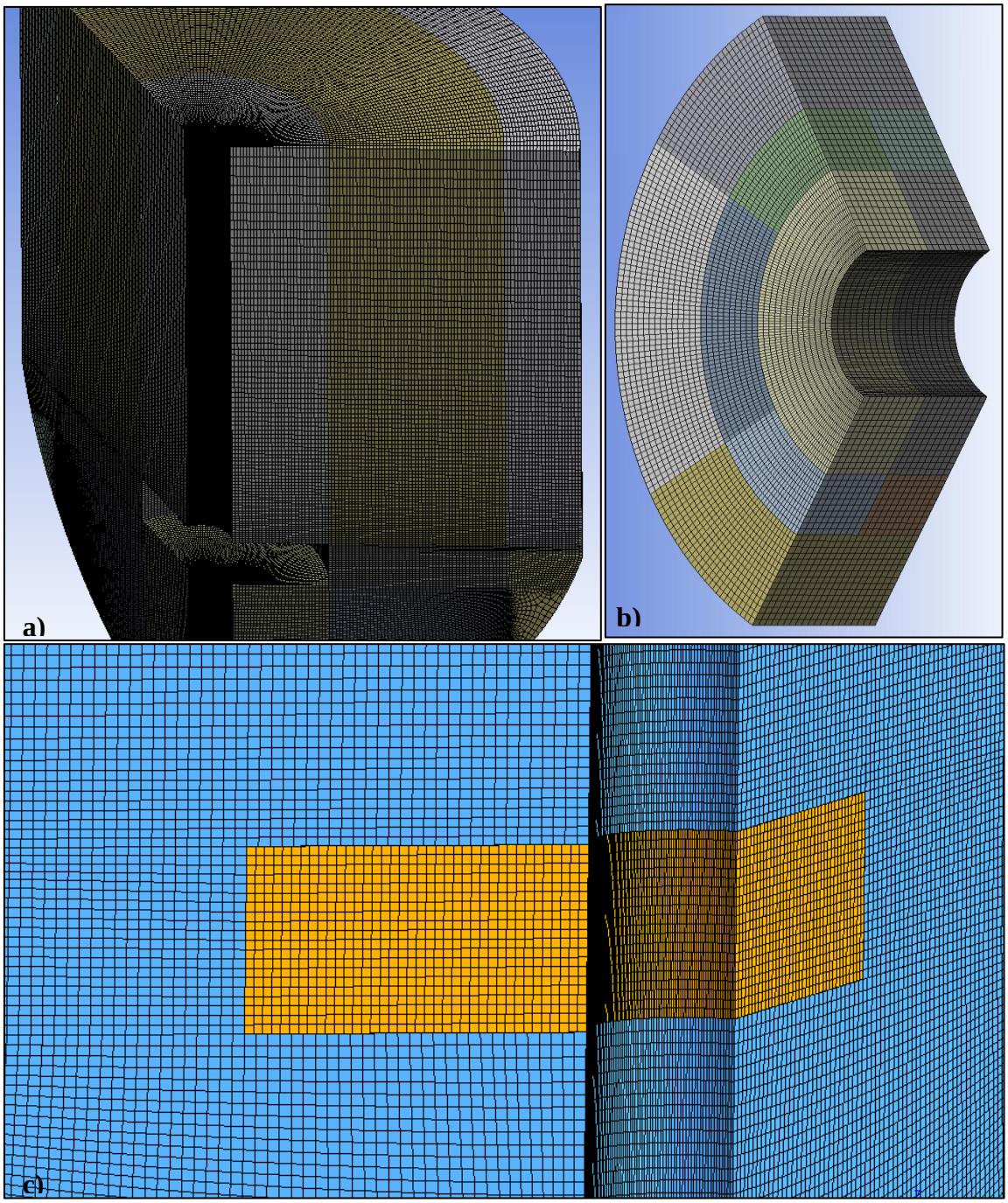

Figure 4-2: Mesh of (a) stirred tank alone, (b) impeller alone, and (c) both tank and impeller together.

4.2 Results and Discussion

In Figure 4-3, the variation of the turbulence energy dissipation rate as a function of rotational speed can be seen. The turbulence energy dissipation rate increases exponentially with an increase in the rotational speed. Similar values for the turbulence

energy dissipation rate were found by Mollet *et al.* (2004) at similar rotational speeds in a geometrically similar stirred tank but with four baffles instead of the three baffles used in this study.

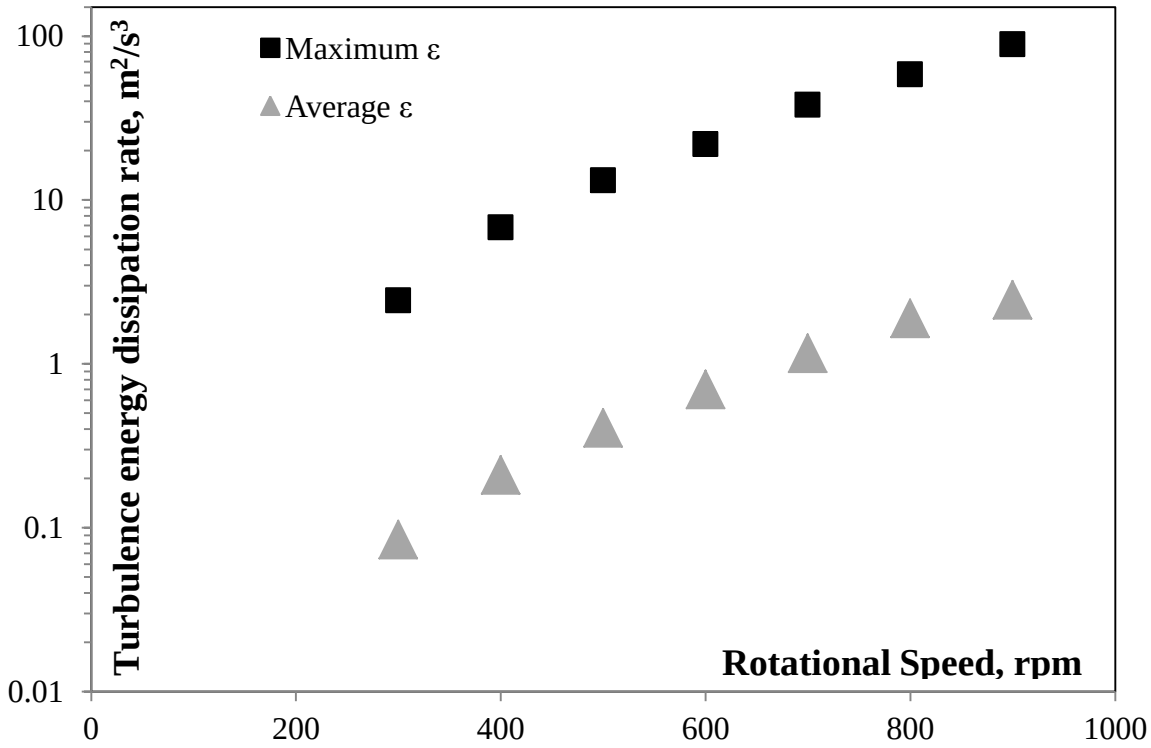

Figure 4-3: Maximum and average turbulence energy dissipation rate as a function of rotational speed estimated by the SST-CC model.

The maximum turbulence energy dissipation rate simulated at 900 rpm of 8.9×10^{1} m^2/s^3 is significantly lower than the maximum turbulence energy dissipation rate of 1.98×10^{5} m^2/s^3 at which Ma *et al.* (2002) observed around 15 % cell damage for the CHO and Sf-9 cell lines and 4 % cell damage for the Hybridoma cell lines. This could imply that very little damage to cells due to turbulence and shear generated by the impeller would occur within the stirred tank tested in this work for rotational speeds of up to 900 rpm. Note, in a bubbled stirred tank, an additional source of turbulence and shear would come from the rising and bursting of bubbles, although the contribution of this effect on the overall turbulence energy dissipation rate has not been quantified in this work. In addition, the difference in percentage cell damage for a given turbulence energy dissipation rate measured by Mollet *et al.* (2008) indicates that optimal operating conditions need to be changed for different cell lines. This implies that separate correlations relating cell death to turbulence energy dissipation rate would need to be developed for different cell lines.

Another point to note is that the residence times of the cells in the vicinity of maximum turbulence energy dissipation rate (close to the impeller) in a stirred tank is similar to the residence times in the contractional flow devices used by Ma *et al*. (2002). However, the cells would undergo multiple exposures to the region of maximum turbulence energy dissipation rate as they circulate within the stirred tank reactor, whereas in the contractional flow device, the cells were exposed to the maximum turbulence energy dissipation rate of 1.98×10^{5} m^2/s^3 only once.

Smith and Greenfield (1992) have shown that they were not able to culture cells without significant cell damage in a geometrically similar stirred tank as tested in this study, above a Reynolds number of 25,000 or a rotational speed of 700 rpm. If the CFD results of this study are used for the stirred tank used by Smith and Greenfield (1992) (due to geometrical similar vessel), then it can be seen that 700 rpm corresponds to the maximum turbulence energy dissipation rate of around 3.8×10^{1} m^2/s^3, which is significantly lower than the maximum turbulence energy dissipation rate of 1.98×10^{5} m^2/s^3 at which Ma *et al*. (2002) observed less than 15 % cell damage for Sf-9 and CHO cell lines and 4% for the Hybridoma cell line. It seems likely that, in the case of multiple exposures for a cell in the vicinity of high level of turbulence energy dissipation rate, such as occurs due to circulation in a stirred tank, the maximum turbulence energy dissipation rate that cells can withstand without significant damage will be significantly less.

The future work of this study will aim to answer this question by doing experiments with animal cell cultures at different rotational speeds while oxygenating through a gas-permeable membrane, so that cell damage only occurs due to shear generated by the impeller. In addition, experiments will be done at different rotational speeds with oxygenation via air-bubbling. These two sets of experiments will be used to separate and quantify cell damage that occurs in a stirred tank reactor due to shear generated by agitation and by the rising and bursting of bubbles.

4.3 Nomenclature

D_a	Diameter of the impeller
D_t	Diameter of the tank
E	Height of the location of the Impeller blade from the bottom of the tank
J	Width of the baffles
H	Height of the tank
L	Length of the blade
W	Width of the blade

5 Conclusions

Shear stress is believed to be the main factor causing cell damage/death during culturing of cells. In stirred tanks, such shear stress results from rising and bursting of bubbles and agitation due to the rotation of the impeller. For stirred tanks, several parameters linked to shear stress have been correlated with cell damage, such as impeller speed, impeller tip velocity, Kolmogorov eddy length scale and turbulence energy dissipation rate. However, it can be argued that turbulence energy dissipation rate is the most appropriate parameter to relate to cell damage since it is not geometry specific, it is general in nature, and intrinsic to any moving fluid. This parameter is difficult to measure experimentally, but it can be predicted locally throughout a reactor using CFD. Various studies have been carried out on cell damage as a function of turbulence energy dissipation rate, but in vessels other than stirred tanks. At present, there is no literature available regarding the use of turbulence energy dissipation rate, predicted numerically via CFD, to estimate cell damage in stirred tanks.

The first part of this study focussed on validating a CFD model for accurately predicting turbulence energy dissipation rate in a stirred tank. The second part of the study investigated appropriate oxygenation rates for culturing cells in a stirred tank, using either air bubbling or gas-permeable membranes. In the third part of the study, the stirred tank used in the oxygenation experiments was modelled using CFD to predict the local turbulence energy dissipation rates. Future studies would focus on correlating the turbulence energy dissipation rate, predicted using CFD, with cell damage measured experimentally within the stirred tank. In such a study, the effects of cell damage due to bubbling and impeller agitation would be separated by using gas permeable membranes for oxygenation to avoid the damaging effects of bubbling. In the first part of this work, a CFD model of a cylindrical tank agitated by a Rushton turbine was validated using experimental data available in the literature. The turbulence models tested were the k-ε, SST, SST-CC, SAS-SST and SSG-RSM turbulence models. All the tested turbulence models predicted the mean axial and tangential velocities reasonably well, but they tended to under-predict the decay of mean radial velocity away from the impeller. The k-ε model poorly predicted the random and periodic components of the kinetic energy of fluctuating motions in the vicinity of the impeller. Furthermore, the predicted trailing vortices were

too short and there were no secondary vortex motions. This model also wrongly predicted the location of the maxima of both the turbulence (random) kinetic energy and turbulence energy dissipation rate at the impeller-tip, whereas experimental results show that the maxima occurs at a dimensionless radial distance of around 1.4 from the impeller axis. The SST model predicted the magnitude of these maxima in reasonable agreement with the experimental findings, and curvature correction helped in improving the predicted location of the maximum. However, both the SST and SST-CC models predicted overly-dissipative trailing vortices that were too short and without the presence of secondary vortex motions, similar to the k-ε model.

The SAS-SST model predictions of periodic and turbulence (random) kinetic energy provided qualitative and quantitative agreement with experiment similar to both the SST and SST-CC turbulence models. Moreover, this model predicted long trailing vortices with secondary motions, as observed experimentally by other researchers. However, the predictions of the turbulence energy dissipation rate were not as good as those of the SST and SST-CC turbulence models, although further refinements of the mesh were required to make a proper assessment of the accuracy of the SAS-SST model. Such refinement proved impractical in this work due to limitations on the computer power available and the significant number of revolutions required to obtain good statistical averages of the turbulence parameters. The SSG-RSM model reproduced the experimental velocity flow fields well and predicted trailing vortices similar in length to the SAS-SST model, however the prediction of the periodic and turbulence (random) kinetic energy and the turbulence energy dissipation rate were poor, and no secondary motions were predicted in the trailing vortices. Overall, the SST model with curvature correction, SST-CC, was the most satisfactory turbulence model tested for predicting turbulent flow in baffled stirred tanks, in terms of both computing time and most accurately predicting the location and magnitude of the turbulence energy dissipation rate.

For all turbulence models tested, the predicted power number determined by integration of the turbulence energy dissipation rate over the tank was likely to be under-predicted and was significantly lower than that calculated using the impeller torque. In order to accurately predict the power number using the impeller torque, the thickness of the blade must be accounted for and resolved properly by the mesh in the simulations. However, this

was impractical in this work due to limitations on the computer power available to produce such a fine mesh.

In the second part of this work, oxygen mass transfer experiments were conducted in a tank stirred with a Rushton turbine using air-bubbling and a gas-permeable membrane as two different methods of oxygenation. The aim of these experiments was to understand the transfer of oxygen at different gas flow rates and impeller rotational speeds for both air-bubbling and permeable-membrane oxygenation in order to find suitable operating conditions for culturing cells in the stirred tank using either method of oxygenation. It was found that the oxygen transfer rate for the gas-permeable membrane was at least 10 times lower than for air-bubbling at the same impeller rotational speeds. The oxygen transfer rates for air-bubbling, even at the lowest reasonable gas flow rate of 0.15 L/min and an oxygen concentration of 21% in the stirred tank, was at least two times higher than the oxygen transfer rate for the gas-permeable membrane at a gas flow rate of 4 L/min and oxygen concentration of 40% in the gas flow rate.

The minimum oxygen requirements for culturing Sf-9 cells, which is a cell line that could be used in future studies for investigating the effect of shear on cell damage/death, is 1 hr^{-1}. In this study, an oxygen transfer rate of at least 2 hr^{-1} was achieved for both air-bubbling and gas-permeable membrane oxygenation, which implies that Sf-9 cells could be successfully cultured in the stirred tank of this study using either method of oxygenation.

In the final part of this study, the stirred tank reactor employed in the oxygenation experiments was modelled with CFD using the SST-CC turbulence model, which was shown in the first part of the study to accurately predict the turbulence energy dissipation rate within a stirred tank. Turbulence energy dissipation rate increased exponentially with an increase in the impeller rotational speed from 300 to 900 rpm. The local maximum turbulence energy dissipation rate of around 8.9×10^{1} m^2/s^3 observed at a rotational speed of 900 rpm, was found to be considerably lower than the local maximum turbulence energy dissipation rate of 1.98×10^{5} m^2/s^3 at which Ma *et al.* (2002) observed up to 15 % cell damage for Sf-9 and CHO cell lines and 4% for the Hybridoma cell line. The cell cultures of Ma *et al.* (2002) were tested in a transient flow contractional device with residence times similar to a stirred tank having a rotational speed of 500 rpm. However, these cells were exposed to high levels of turbulence energy dissipation rates only once.

The cells in a stirred tank are exposed multiple times to high levels of turbulence energy dissipation rate in the vicinity of the impeller due to the circulatory nature of the flow. Thus, the value of maximum turbulence energy dissipation rate that a cell can withstand would be substantially lower in a stirred tank than in a single-pass flow device, since the integrated exposure time is considerably longer. Clearly, both the residence time of a single pass and the number of exposures to high turbulence energy dissipation rate in the vicinity of the impeller must be considered when estimating cell damage in a stirred-tank reactor.

For a geometrically similar stirred tank and Rushton turbine to the one used in this study, cells were cultured successfully without significant damage at a rotational speed of 600 rpm with headspace gassing as the oxygenation method by Smith and Greenfield (1992).

This study can be used as a starting point for creating a model for estimating cell damage in different types and scales of reactors. In this regard, future work would involve detailed cell-culture experiments in a stirred-tank reactor at different impeller rotational speeds with the two different methods of oxygenation: air-bubbling and permeable membrane oxygenation. One experiment would be conducted to quantify the effect of agitation on cell damage/death. In this experiment, cells would be cultured in a stirred tank reactor at different agitation rates using a gas-permeable membrane for oxygenation to eliminate cell damage normally associated with bubbling. Another experiment would be conducted to quantify the effect of bursting bubbles on animal cells by comparing the experimental results of two different methods of oxygenation, air-bubbling and gas-permeable membranes, for a given impeller rotational speed. The data sets of both these experiments would be brought together to develop correlations that relate cell damage/death to turbulence energy dissipation rate (as related to agitation) and bubbling rates. The results of these experiments would also help elucidate the importance of residence time in the vicinity of high turbulence energy dissipation rate and multiple exposures to that high value on the culturing of cells in stirred tank reactors. Different animal cell cultures would also be tested, especially those which are most commonly used in industry, such as Sf-9, Hybridoma and CHO cell lines, in order to establish the optimal operating parameters for the most commonly used cultures for industrial use.

The next step of the study would be to produce cell cultures in different scales of reactor to show that the developed cell damage/death correlations can be applied to any scale of reactor. This would demonstrate that these correlations are useful to determine appropriate impeller rotational speeds and bubbling rates that minimize cell damage in any scale of reactor.

6 References

Abu-Reesh, I., & Kargi, F. (1989). Biological responses of hybridoma cells to defined hydrodynamic shear stress. *Journal of Biotechnology, 9*, 913-919.

Ahmed, T., Semmens, M. J., & Voss, M. A. (2004). Oxygen transfer characteristics of hollow-fiber, composite membranes. *Advances in Environmental Research, 8*(3-4), 637-646.

ANSYS-CFX. (2009) (Version 12.1) [Computational Fluid Dynamics]: http://www.ansys.com/.

Aubin, J., Fletcher, D. F., & Xuereb, C. (2004). Modeling turbulent flow in stirred tanks with CFD: the influence of the modeling approach, turbulence model and numerical scheme. *Experimental Thermal and Fluid Science, 28*(5), 431-445.

Bakker, A., Myers, K. J., Ward, R. W., & Lee, C. K. (1996). The laminar and turbulent flow pattern of a pitched blade turbine. *Chemical Engineering Research and Design, 74*(A4), 485-491.

Bakker, A., & Oshinowo, L. M. (2004). Modelling of turbulence in stirred vessels using large eddy simulation. *Chemical Engineering Research and Design, 82*(9), 1169-1178.

Bates, R. L., Fondy, P. L., & Corpstein, R. R. (1963). An examination of some geometric parameters of impeller power. *Industrial & Engineering Chemistry Process Design and Development, 2*(4), 310-314.

Brucato, A., Ciofalo, M., Grisafi, F., & Micale, G. (1998). Numerical prediction of flow fields in baffled stirred vessels: A comparison of alternative modelling approaches. *Chemical Engineering Science, 53*(21), 3653-3684.

Chisti, Y. (2001). Hydrodynamic damage to animal cells. *Critical Reviews in Biotechnology, 21*, 67-110.

Coroneo, M., Montante, G., Paglianti, A., & Magelli, F. (2010). CFD prediction of fluid flow and mixing in stirred tanks: Numerical issues about the RANS simulations. *Computers & Chemical Engineering, In Press, Corrected Proof*, 10.

Cutter, L. A. (1966). Flow and turbulence in a stirred tank. *American Institute of Chemical Engineers. AIChE Journal, 12*(1), 35-45.

Deglon, D. A., & Meyer, C. J. (2006). CFD modelling of stirred tanks: numerical considerations. *Minerals Engineering, 19*(10), 1059-1068.

Delafosse, A., Liné, A., Morchain, J., & Guiraud, P. (2008). LES and URANS simulations of hydrodynamics in mixing tank: comparison to PIV experiments. *Chemical Engineering Research and Design, 86*(12), 1322-1330.

Derksen, J., & Van den Akker, H. E. A. (1999). Large eddy simulations on the flow driven by a Rushton turbine. *American Institute of Chemical Engineers. AIChE Journal, 45*, 209-221.

Derksen, J. J., Doelman, M. S., & Van den Akker, H. E. A. (1999). Three-dimensional LDA measurements in the impeller region of a turbulently stirred tank. *Experiments in Fluids, 27*(6), 522-532.

Ducci, A., & Yianneskis, M. (2005). Direct determination of energy dissipation in stirred vessels with two-point LDA. *American Institute of Chemical Engineers. AIChE Journal, 51*(8), 2133-2149.

Escudié, R., & Liné, A. (2003). Experimental analysis of hydrodynamics in a radially agitated tank. *American Institute of Chemical Engineers. AIChE Journal, 49*(3), 585-603.

Escudié, R., & Liné, A. (2006). Analysis of turbulence anisotropy in a mixing tank. *Chemical Engineering Science, 61*(9), 2771-2779.

Frank, T., Prasser, H. M., Menter, F., & Lifante, C. (2010). Simulation of turbulent and thermal mixing in T-junctions using URANS and scale-resolving turbulence models in ANSYS CFX. *Nuclear Engineering and Design, 240*(9), 2313-2328.

Garcia-Briones, M. A., & Chalmers, J. J. (1994). Flow parameters associated with hydrodynamic cell injury. *Biotechnology and Bioengineering, 44*, 1089-1098.

Gregoriades, N., Clay, J., Ma, N., Koelling, K., & Chalmers, J. J. (2000). Cell damage of microcarrier cultures as a function of local energy dissipation created by a rapid extensional flow. *Biotechnology and Bioengineering, 69*(2), 171-182.

Hartmann, H., Derksen, J. J., Montavon, C., Pearson, J., Hamill, I. S., & van den Akker, H. E. A. (2004). Assessment of large eddy and RANS stirred tank simulations by means of LDA. *Chemical Engineering Science, 59*(12), 2419-2432.

Heller, J., Pasternak, R. A., & Christensen, M. V. (1970). Diffusion and permeation of oxygen, nitrogen, carbon dioxide, and nitrogen dioxide through polytetrafluoroethylene. *Macromolecules, 3*(3), 366-371.

Honkanen, M., Vaittinen, J., Saarenrinne, P., & Korpijärvi, J. (2007, September 11-14, 2007). *Time-resolved stereoscopic PIV experiments for validating transient CFD simulations.* Paper presented at the 7th International Symposium on Particle Image Velocimetry, Roma, Italy, September 11-14, 2007.

Jahoda, M., Mostek, M., Kukuková, A., & Machon, V. (2007). CFD modelling of liquid homogenization in stirred tanks with one and two Impellers using large eddy simulation. *Chemical Engineering Research and Design, 85*(5), 616-625.

Javed, K. H., Mahmud, T., & Zhu, J. M. (2006). Numerical simulation of turbulent batch mixing in a vessel agitated by a Rushton turbine. *Chemical Engineering and Processing, 45*(2), 99-112.

Jones, R. M., Harvey III, A. D., & Acharya, S. (2001). Two-equation turbulence modeling for impeller stirred tanks. *Journal of Fluids Engineering, 123*, 640-648.

Joshi, J. B., Elias, C. B., & Patole, M. S. (1996). Role of hydrodynamic shear in the cultivation of animal, plant and microbial cells. *The Chemical Engineering Journal 62*, 121-141.

Kunas, K. T., & Papoutsakis, E. T. (1990). Damage mechanisms of suspended animal cells in agitated bioreactors with and without bubble entrainment. *Biotechnology and Bioengineering, 36*(5), 476-483.

Lee, K. C., & Yianneskis, M. (1998). Turbulence properties of the impeller stream of a Rushton turbine. *American Institute of Chemical Engineers. AIChE Journal, 44*(1), 13-24.

Lynch, W. (1978). *Handbook of Silicon Rubber Fabrication*. New York: Van Nostrand Reinhold.

Ma, N., Koelling, K. W., & Chalmers, J. J. (2002). Fabrication and use of a transient contractional flow device to quantify the sensitivity of mammalian and insect cells to hydrodynamic forces. *Biotechnology and Bioengineering, 80*(4), 428-437.

Mavros, P. (2001). Flow visualization in stirred vessels: A review of experimental techniques. *Chemical Engineering Research and Design, 79*(2), 113-127.

Menter, F. R. (1994). Two-equation eddy-viscosity turbulence models for engineering applications. *AIAA Journal, 32*, 1598-1605.

Menter, F. R. (2009). Review of the shear-stress transport turbulence model experience from an industrial perspective. *International Journal of Computational Fluid Dynamics, 23*(4), 305 - 316.

Menter, F. R., & Egorov, Y. (2005). *A scale-adaptive simulation model using two-equation models.* Paper presented at the 43rd AIAA Aerospace Sciences Meeting and Exhibit, January 10, 2005 - January 13, 2005, Reno, NV, United states.

Mills, A. F. (1999). *Basic heat and mass transfer*. Upper Saddle River, N.J: Prentice Hall.

Mollet, M., Godoy-Silva, R., Berdugo, C., & Chalmers, J. J. (2007). Acute hydrodynamic forces and apoptosis: A complex question. *Biotechnology and Bioengineering, 98*(4), 772-788.

Mollet, M., Godoy-Silva, R., Berdugo, C., & Chalmers, J. J. (2008). Computer Simulations of the energy dissipation rate in a fluorescence-activated cell sorter: Implications to cells. *Biotechnology and Bioengineering, 100*(2), 260-272.

Mollet, M., Ma, N., Zhao, Y., Brodkey, R., Taticek, R., & Chalmers, J. J. (2004). Bioprocess equipment: Characterization of energy dissipation rate and its potential to damage cells. *Biotechnology Progress, 20*(5), 1437-1448.

Montante, G., Lee, K. C., Brucato, A., & Yianneskis, M. (2001). Numerical simulations of the dependency of flow pattern on impeller clearance in stirred vessels. *Chemical Engineering Science, 56*(12), 3751-3770.

Murthy, B. N., & Joshi, J. B. (2008). Assessment of standard k-ε, RSM and LES turbulence models in a baffled stirred vessel agitated by various impeller designs. *Chemical Engineering Science, 63*(22), 5468-5495.

Ng, K., Fentiman, N. J., Lee, K. C., & Yianneskis, M. (1998). Assessment of sliding mesh CFD predictions and LDA measurements of the flow in a tank stirred by a Rushton impeller. *Chemical Engineering Research and Design, 76*(6), 737-747.

Rushton, J. H., Costich, E. W., & Everett, H. J. (1950). Power characteristics of mixing impellers. *Chemical Engineering Progress, 46*(9), 467-476.

Rutherford, K., Lee, C. K., Mahmoudi, S. M., & Yianneskis, M. (1996). Hydrodynamic characteristics of dual Rushton impeller stirred vessels. *American Institute of Chemical Engineers. AIChE Journal, 42*(2), 332-346.

Rutherford, K., Mahmoudi, S. M., Lee, K. C., & Yianneskis, M. (1996). The influence of Rusthon impeller blade and disk thickness on the mixing charasteristics of stirred vessels. *Trans IChemE, 74*(A), 369-378.

Schneider, M., Reymond, F., Marison, I. W., & Vonstockar, U. (1995). Bubble free oxygenation by means of hydrophobic porous membranes. *Enzyme and Microbial Technology, 17*(9), 839-847.

Sheng, J., Meng, H., & Fox, R. O. (1998). Validation of CFD simulations of a stirred tank using particle image velocimetry data. *Canadian Journal of Chemical Engineering, 76*, 611-625.

Singh, V. (1999). Disposable bioreactor for cell culture using wave-induced agitation. *Cytotechnology, 30*(1-3), 149-158.

Smirnov, P. E., & Menter, F. R. (2009). Sensitization of the SST turbulence model to rotation and curvature by applying the Spalart-Shur correction term. *Journal of Turbomachinery, 131*(4), 1-8.

Smith, C. G., & Greenfield, P. F. (1992). Mechanical agitation of hybridoma suspension cultures: Metabolic effects of serum, pluronic F68, and albumin supplements. *Biotechnology and Bioengineering, 40*(9), 1045-1055.

Spalart, P. R., & Shur, M. (1997). On the sensitization of turbulence models to rotation and curvature. *Aerospace Science and Technology, 1*(5), 297-302.

Speziale, C. G., Sarkar, S., & Gatski, T. B. (1991). Modelling the pressure-strain correlation of turbulence: an invariant dynamical systems approach. *Journal of Fluid Mechanics, 227*, 245-272.

Tramper, J., Williams, J. B., Joustra, D., & Vlak, J. M. (1986). Shear sensitivity of insect cells in suspension. *Enzyme and Microbial Technology, 8*(1), 33-36.

Vladisavljevic, G. T. (1999). Use of polysulfone hollow fibers for bubbleless membrane oxygenation/deoxygenation of water. *Separation and Purification Technology*, *17*(1), 1-10.

Voss, M. A., Ahmed, T., & Semmens, M. J. (1999). Long-term performance of parallel-flow, bubbleless, hollow-fiber-membrane aerators. *Water Environment Research, 71*(1), 23-30.

Wilderer, P. A., Bräutigam, J., & Sekoulov, I. (1985). Application of gas permeable membranes for auxiliary oxygenation of sequencing batch reactors. *Conservation & Recycling, 8*(1-2), 181-192.

Wu, H., & Patterson, G. K. (1989). Laser-doppler measurements of turbulent-flow parameters in a stirred mixer. *Chemical Engineering Science, 44*(10), 2207-2221.

Wu, J., & Goosen, M. F. A. (1995). Evaluation of the killing volume of gas bubbles in a sparged animal cell culture bioreactors. *Enzyme and Microbial Technology*, *17*, 1036-1042.

Yeoh, S. L., Papadakis, G., & Yianneskis, M. (2004). Numerical simulation of turbulent flow characteristics in a stirred vessel using the LES and RANS approaches with the sliding/deforming mesh methodology. *Chemical Engineering Research and Design, 82*(7), 834-848.

Zadghaffari, R., Moghaddas, J. S., & Revstedt, J. (2010). Large-eddy simulation of turbulent flow in a stirred tank driven by a Rushton turbine. *Computers & Fluids*, *39*(7), 1183-1190.

Zhang, Y., Yang, C., & Mao, Z. (2006). Large eddy simulation of liquid flow in a stirred tank with improved inner-outer iterative algorithm. *Chinese Journal of Chemical Engineering, 14*(3), 321-329.

7 Appendix

7.1 Measurement of saturated concentration of oxygen in water at different oxygen concentrations in air.

$$K_{h,c_a}^{p_g} = P_g / c_a$$

Formula for linear averaging	
slope	(y1-y2)/(x1-x2)
y3	slope × (X3-X2) + Y2

Henry's constant in Pis/Xiu in atm source Mills, A.F. (1999)						
Temp (K)	290	293	298	300	310	320
Solute/Temp (C)	ε17	20	25	27	37	47
O2	38000	40100	43600	45000	52000	57000
Air	62000	65600	71600	74000	84000	92000

$$K_H = \rho_{H_2O} / (M_{H_2O} \cdot K_{H,c_a}^{P_g})$$

Density of water, 20 C			998.2	kg/m^3	g/L	
Molecular mass of water			18.0	g/mole		
K_H						
Solute/Temp (K)	290	293	298	300	310	320
O2	0.00146	0.00138	0.00127	0.00123	0.00107	0.00097
Air	0.00089	0.00084	0.00077	0.00075	0.00066	0.00060

Component	Fractions	Fractions	Fractions	Fractions
Air	1	1	1	1
Oxygen	0.21	0.30	0.40	0.50
Nitrogen	0.79	0.70	0.60	0.50

	Total Pressure, air	
S.No	bar	atm
1	1	0.99
2	1.21	1.19

$$K_H = c_a / p_g$$

Total Pressure of air × fraction of oxygen

Saturated concentration of 21% oxygen in water, C_a in case of bubbling in mg/L						
Temp(K)	290	293	298	300	310	320
Pressure (bar)/Temp (C)	17	20	25	27	37	47
1	9.7	9.2	8.4	8.2	7.1	6.4
1.21	11.7	11.1	10.2	9.9	8.6	7.8

Saturated concentration of 30% oxygen in water, C_a in case of bubbling in mg/L						
Temp(K)	290	293	298	300	310	320
Pressure (bar)/Temp (C)	17	20	25	27	37	47
1	13.8	13.1	12.0	11.7	10.1	9.2
1.21	16.7	15.8	14.6	14.1	12.2	11.1

Saturated concentration of 40% oxygen in water, C_a in case of bubbling in mg/L						
Temp(K)	290	293	298	300	310	320
Pressure (bar)/Temp (C)	17	20	25	27	37	47
1	18.4	17.5	16.1	15.6	13.5	12.3
1.21	22.3	21.1	19.4	18.8	16.3	14.9

P_g at 21 % O_2			
Partial pressure, O_2		Partial pressure, N_2	
bar	Atm	bar	atm
0.21	0.21	0.79	0.78
0.25	0.25	0.96	0.94
Pg at 30 % O2			
Partial pressure, O_2		Partial pressure, N_2	
bar	Atm	bar	atm
0.30	0.30	0.70	0.69
0.36	0.36	0.85	0.84
Pg at 40 % O2			
Partial pressure, O_2		Partial pressure, N_2	
bar	Atm	bar	atm
0.40	0.39	0.60	0.59
0.48	0.48	0.73	0.72
Pg at 50 % O2			
Partial pressure, O_2		Partial pressure, N_2	
bar	atm	bar	atm
0.50	0.49	0.50	0.49
0.61	0.60	0.61	0.60

7.2 Measurement of Concentration C_1 for gas-permeable membrane.

The molar concentration of oxygen in water could not be measured directly. The dissolved oxygen probe measures only in percentage oxygen saturation. In addition, the break-down of the three different resistances (gas-side, liquid side and membrane resistance) of the gas-permeable membrane is difficult to estimate without knowing the solubility of oxygen in the membrane. To estimate the oxygen concentration C_1, a set of experiments was done, in which, initially, 0-100% for the oxygen probe was calibrated in an air bubbling experiment. Nitrogen was bubbled through the stirred tank to strip the water of oxygen, reducing the oxygen concentration to 0%, at which point the oxygen probe was calibrated to 0%. Then air was bubbled to increase the oxygen concentration in water to 100%, at which point the oxygen probe was calibrated to 100%. With this calibration of the extremes completed, nitrogen was then used to strip oxygen from the water once again. Then, the gas-permeable membrane was used to oxygenate the water. Note that the oxygen probe kept the same calibration as set in the air bubbling experiment. A concentration of virtually 100% was eventually reached when using the gas-permeable membrane, as shown in Figure 7-1. This suggests that the oxygen concentration C_1 should be set to C_{Asat} concentration, as in the case of the air-bubbling experiments.

The saturation concentration of oxygen increases from 9.2 mg/L at 21% oxygen concentration in the gas phase, to 13.1 mg/L at 30% oxygen concentration in the gas phase (pressure of 1 bar and temperature of 20^{o}C) as shown in Appendix 7.1. This signifies that the percentage increase in the saturation concentration of oxygen in water (as measured by the dissolved oxygen probe calibrated using the method described above) when the concentration of oxygen in the gas phase is increased from 21% to 30% oxygen concentration, should be approximately 142.9 % (13.1/9.2x100%). Under similar conditions of 30 % oxygen concentration in the gas flow rate (pressure of 1 bar and temperature of 20^{o}C) using the gas-permeable membrane, the oxygen probe detected a saturated concentration of oxygen of 143% in the stirred tank. Similar observations were made in the case of 40 % oxygen concentration in the gas flow rate. Oxygen probe detected a saturated concentration of oxygen of 189 % in the stirred tank, and the concentration of the oxygen in the gas phase, when oxygen concentration is increased

from 21% to 40%, should be approximately 190.2 % (17.5/9.2×100). Thus, it can be seen that the oxygen concentration C_1 is equal to C_{Asat} concentration within the 2.1% error in the measurement of oxygen transfer rate with the gas-permeable membrane.

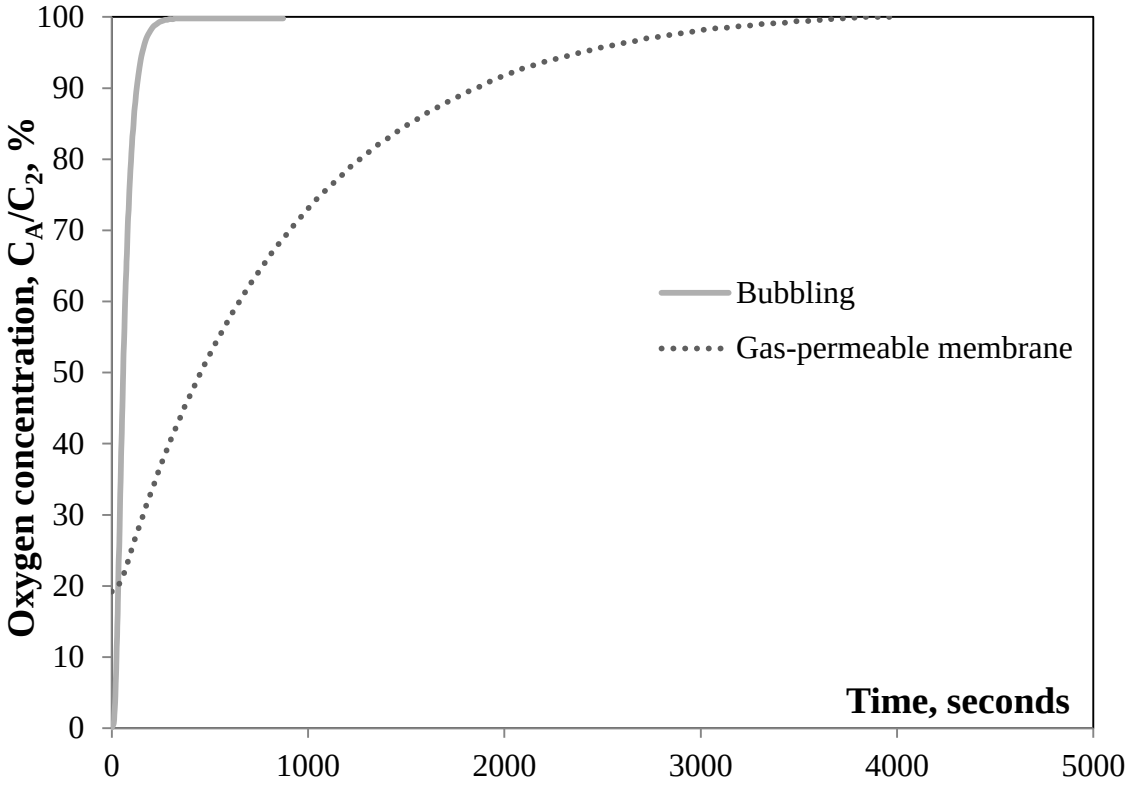

Figure 7-1: Oxygen probe response for oxygen concentration measurements at a rotational speed of 400 rpm and gas flow rate of 4 L/min for air-bubbling and gas-permeable membrane.

7.3 Oxygen transfer rate calculations of bubbling experiments

Gas flow rate = 4 L/min			
C_{A0}	0.1	%	
C_{Asat}	100	%	
Rotational speed = 700 rpm			
Time	Conc., C_A	Time	ln term
Sec	%	sec	(-)
0	0.1	0	0.000
10	0.7	10	0.006
13	1.9	13	0.018
17	3.6	17	0.036
19	5.3	19	0.053
20	6.3	20	0.064
22	7.8	22	0.080
23	8.9	23	0.092
24	10.1	24	0.105
25	11.4	25	0.120
27	12.8	27	0.136
28	14.3	28	0.153
30	16.0	30	0.173
31	17.7	31	0.194
32	19.0	32	0.210
33	20.5	33	0.228
34	22.0	34	0.247
35	23.5	35	0.267
38	25.5	38	0.293
39	26.8	39	0.311
40	28.2	40	0.330
41	29.8	41	0.353
42	31.4	42	0.376
43	33.0	43	0.399
45	34.7	45	0.425
46	36.2	46	0.448
47	37.6	47	0.471
48	39.0	48	0.493
51	41.5	51	0.535

$$ln\frac{(C_{Asat} - C_{A0})}{(C_{Asat} - C_A)}$$

Note 1: The oxygen probe used in the experiments calculates only in percentages.

Note 2: Because C_A can reach the C_{Asat} concentration in the case of bubbling experiments, the concentrations were not converted to mg/L from percentages

7.4 Oxygen transfer rate calculations of gas-permeable membrane experiments

Gas flow rate = 4 L/min			
C_0	0.2	%	
C_1	100	%	
300 rpm			
Time	Conc. C_2	Time	ln term
Sec	%	Sec	(-)
0	0.2	0	0
27	0.3	27	0.001
37	0.6	37	0.00402
47	1.0	47	0.00805
57	1.5	57	0.01311
67	2.1	67	0.01922
77	2.6	77	0.02434
87	3.2	87	0.03052
97	3.8	97	0.03674
107	4.5	107	0.04404
117	5.2	117	0.0514
127	5.8	127	0.05775
137	6.4	137	0.06414
147	7.1	147	0.07164
157	7.7	157	0.07812
167	8.3	167	0.08465
177	9.0	177	0.09231
187	9.6	187	0.09892
197	10.3	197	0.1067
207	10.9	207	0.11341
217	11.5	217	0.12017
227	12.1	227	0.12697
237	12.7	237	0.13382
247	13.3	247	0.14071
257	14.0	257	0.14882
267	14.5	267	0.15465
277	15.2	277	0.16287

Note 1: The oxygen probe used in the experiments only calculates in percentages.

Note 2: Appendix 3.1 shows that C_2 can reach the C_{Asat} concentration in the case of gas-permeable membrane experiments, so the concentrations were not converted to mg/L from percentages.

$$ln\frac{(C_1 - C_0)}{(C_1 - C_2)}$$